CO-sensing Properties of Potentiometric Gas Sensors Using an Anion-conducting Polymer Electrolyte and Au-loaded Metal Oxide Electrodes

Toshiyuki Goto[1], Takeo Hyodo[1], Taro Ueda[1], Kai Kamada[1], Kazunari Kaneyasu[2] and Yasuhiro Shimizu[1,*]

[1]Graduate School of Engineering, Nagasaki University,

1-14 Bunkyo-machi, Nagasaki 852-8521, Japan

[2]Figaro Engineering Inc.,

1-5-11 Senbanishi, Minoo, Osaka 562-8505, Japan

*Corresponding author:

Yasuhiro Shimizu, Prof. Dr.

Graduate School of Engineering, Nagasaki University

1-14 Bunkyo-machi, Nagasaki 852-8521, Japan

Tel: +81-95-819-2642

Fax: +81-95-819-2643

E-mail: shimizu@nagasaki-u.ac.jp

Abstract

CO-sensing properties of potentiometric gas sensors using an anion-conducting polymer (ACP) as an electrolyte and metal oxides loaded with and without Au as electrodes (EC(MO) or EC(*n*Au/MO(*T*m)), respectively, MO: metal oxide (In_2O_3, ZnO or Co_3O_4), *n*: the loading amount of Au, *0.5~2.0* wt%, *T*: heat-treatment temperature, m: heat-treatment atmosphere, air or H_2) have been investigated in wet synthetic air (57%RH) at 30ºC. In addition, H_2-sensing properties of these sensors have also been investigated in the same gaseous conditions, to evaluate their CO selectivity against H_2. All of the EC(MO) sensors showed relatively small changes in electromotive force (EMF), i.e. responses, to both CO and H_2, but the Au loading to In_2O_3 and ZnO drastically improved the magnitude of CO response of the EC(In_2O_3) and EC(ZnO) sensors, respectively. The EC(*2.0*Au/In_2O_3(*400*air)) sensor showed larger CO response, faster CO response speed, excellent CO selectivity against H_2 and better long-term stability than those of the EC(*2.0*Au/ZnO(*400*air)) sensor. The influence of moisture on the CO response of the EC(*2.0*Au/In_2O_3(*400*air)) sensor was almost negligible in the humidity range of 40~100%RH. The magnitude of CO response of the EC(*2.0*Au/In_2O_3(*400*air)) sensor in wet synthetic air showed a good linear relationship with CO concentration, but the CO response was largely affected by the concentration of O_2. These results indicate that the EMF of the EC(*2.0*Au/In_2O_3(*400*air)) sensor is probably determined by the mixed potential resulting from CO oxidation and O_2 reduction. The heat-treatment conditions of the *2.0* wt% Au-loaded In_2O_3 powder largely affected the CO-sensing properties of the EC(*2.0*Au/In_2O_3(*T*m)) sensors. Among these sensors heat-treated in various conditions, the as-fabricated EC(*2.0*Au/In_2O_3(*250*H_2)) sensor showed the most excellent CO selectivity against H_2 in their concentration range of 10~3000 ppm.

***Keywords*:** Gas sensor; Anion-conducting polymer; Carbon monoxide; Gold nanoparticle;

Metal oxide

1. Introduction

Highly conductive anion-conducting polymers (ACP) have recently been developed by some researchers and companies, and their large OH^- conductivities and improved long-term stabilities were quite attractive for an electrolyte of polymer-electrolyte fuel cells (PEFCs) [1-5]. For example, Matsumoto et al. have reported that the PEFCs using an ACP electrolyte showed high current density as well as high power density with relatively low overpotential [6], and their properties except for the long-term stability have been already comparable to those of PEFCs using proton-conducting polymers such as Nafion®, which has been put into practical use. On the other hand, it is well-known that various electrochemical gas sensors using the Nafion® as an electrolyte have also been developed and their sensing properties to some gases were really excellent even at RT [7-12], but to data electrochemical gas sensors using an ACP electrolyte have been rarely reported [13-15]. We have already reported that potentiometric gas sensors employing an ACP electrolyte and Pt- or Pd-loaded carbon black (CB) electrodes showed relatively large responses to CO_2 [16] or H_2 [17], respectively. In addition, we have demonstrated that the sensor employing an ACP as an electrolyte and Pd-loaded CB as an electrode also showed relatively large response to CO [18, 19], but the CO selectivity of the sensor against H_2 was much lower than we expected. However, the potentiometric sensors using the Nafion® also showed that the magnitude of CO response was almost similar to the magnitude of H_2 response at RT [7, 8]. Since CO, which is colorless and scentless, is very harmful to human health directly, relatively high CO sensitivity as well as excellent CO selectivity against other inflammable gases were very important requisites for the application of the CO sensors in various fields. Thus, the CO selectivity of various types of CO sensors has been improved by controlling the composition of the sensing material and

the sensor structure. Sorita et al. reported that the CO selectivity of $LaMnO_3$ against H_2, CH_4, and C_3H_8 was much higher than that of other La-based perovskite-type oxides ($LaMO_3$, M = Fe, Co, and Cr), as a CO-sensing electrode of solid-electrolyte gas sensors (electrolyte: yttria-stabilized zirconia (YSZ)) operating at 400ºC [20], and Miura et al. demonstrated that the combination of SnO_2 and CdO as electrodes of a YSZ-based sensor showed the highest CO selectivity against H_2 at 600ºC, among all oxide materials tested [21]. Takeda et al. also reported that an addition of Bi_2O_3 into a Pt-sensing electrode of a NASICON-based sensor was dramatically improved the CO selectivity against H_2 at RT [22, 23]. SnO_2 mixed with CeO_2 and PdO_x [24], partially-reduced TiO_2 [25], In-doped ZnO [26], CuO-coated Zn_2SnO_4 [27] and Pd/SnO_2 nanocomposite mixed with carbon nanotube [28] were utilized as a promising CO-sensing material for semiconductor gas sensors with high CO selectivity against inflammable gases.

In this study, we have attempted to improve the CO-sensing properties, especially CO selectivity against H_2, of ACP electrolyte-based potentiometric gas sensors by utilizing some kinds of metal oxides (In_2O_3, ZnO and Co_3O_4) as an electrode material. In addition, deposition of Au nanoparticles on the oxide surface was conducted to achieve further improvement of the CO-sensing properties, because it is well-known that the Au nanoparticles deposited on the surface of metal oxides such as TiO_2 α-Fe_2O_3 and Co_3O_4 show an excellent catalytic activity for CO oxidation at low temperatures such as room temperature [29, 30]. Furthermore, the effect of thermal-treatment conditions of Au-loaded oxides and the influence of humidity and oxygen concentration in the gas atmosphere on their CO-sensing properties were also investigated. Based on these results, CO-sensing mechanism has also been discussed.

2. Experimental

2.1. Preparation of metal oxide powders loaded with and without Au

Three kinds of metal oxide powders (MO: In_2O_3, ZnO and Co_3O_4) were prepared according to the following procedure. The pH of 0.35 M $In(NO_3)_3$, 0.34 M $Co(NO_3)_2$ and 0.84 M $Zn(NO_3)_2$ aqueous solutions were adjusted to 3.5, 8.5 and 8.5, respectively, by the addition of an NH_3 aqueous solution. The precipitates obtained were centrifuged and washed with pure water repeatedly, and then dried at 120°C. The MO powders were prepared by the calcination of the resultant dried precipitates at 500°C for 3 h in air. The loading of Au nanoparticles on the MO powders was performed by a general precipitation-deposition method [31]. After the pH of a 1 mM $HAuCl_4$ aqueous solution at 70°C was adjusted to 4 by the addition of a NH_3 aqueous solution, an appropriate amount of one of the MO powders was added to the solution. The pH of the solution was adjusted to 7 by the further addition of the NH_3 aqueous solution and the solution was stirred at 70°C for 1 h, to deposit Au-based precipitates ($Au(OH)_3$) on the surface of the MO powders, and then they were centrifuged and washed with pure water, repeatedly. They were dried at 100°C and then heat-treated at 100, 250 or 400°C for 1 h in air or H_2 to obtain Au-loaded MO powders (*n*Au/MO(*T*m), *n*: the loading amount of Au, 0.5~2 wt%, *T*: heat-treatment temperature, *100*, *250* or *400*, m: heat-treatment atmosphere, air or H_2). The reduction of $Au(OH)_3$ to Au metal by the heat-treatment was clearly confirmed by the change in the color from yellow ($Au(OH)_3$) to violet (Au nanoparticles), which was derived from the surface plasmon resonance [32].

Crystal phases of the MO powders prepared were characterized by X-ray diffraction analysis (XRD; Rigaku Corp., RINT2200) using Cu Kα radiation (40 kV, 36 mA), and their crystallite size was calculated by using Scherrer equation. The pore size distribution and specific surface area (SSA) of the MO powders were measured by general Barrett-Joyner-Halenda (BJH) and Brunauer-Emmett-Teller (BET) methods using N_2 adsorption-desorption isotherms (Micromeritics Inst. Corp., TriStar 3000), respectively.

Morphology of Au particles loaded on the MO powders was observed with a transmission electron microscope (TEM; JEOL Ltd., JEM2010).

2.2. Fabrication of electrochemical gas sensors

A schematic drawing of a sensor element (an electrochemical cell) is shown in Fig. 1(a). The MO or *n*Au/MO(*T*m) powder was mixed with an ACP solution (AS-4, Tokuyama Corp.), which is an *iso*-propanol containing a 5 wt% hydrocarbon-type ionic polymer with quaternary ammonium salts (MO (or *n*Au/MO(*T*m)) : ACP = 95 : 5 in weight). The paste obtained was applied on the surface of both sides of an ACP membrane (A201, Tokuyama Corp., a polyolefin polymer film which consists of hydrocarbon main chain and quaternary ammonium salts) as sensing and counter electrodes by screen printing, and then it was dried at ca. 50°C for 30 min. The sensor element fabricated with MO or *n*Au/MO(*T*m) powder was denoted as EC(MO) or EC(*n*Au/MO(*T*m)), respectively. The surface morphology and thickness of the electrode were observed with a scanning electron microscope (SEM; JEOL Ltd., JCM-5700).

2.3. Gas-sensing measurement

A schematic drawing of a gas-sensing measurement system with two electrode compartments is shown in Fig. 1(b). The sensor element fabricated was sandwiched with Au meshes as a current collector and was set up in a gas-sensing measurement system with two electrode compartments which allowed us to flow different gases over sensing- and counter-electrodes. Gas-sensing properties of all sensors were evaluated by measuring the electromotive force (EMF) at 30°C by flowing CO or H_2 balanced with synthetic air (O_2: 20%, N_2: 80%) over the sensing-electrode, while synthetic air was flown over the counter-electrode. Relative humidity (RH) at both the SE and the CE sides was controlled to be 0~100% at 30°C.

The magnitude of response was defined as a change in EMF induced by a sample gas (ΔEMF_{SG}, SG (sample gas): CO or H_2). The CO selectivity against H_2 was defined as the ratio of CO response to H_2 response ($\Delta EMF_{CO}/\Delta EMF_{H_2}$). The 90% response and recovery times were defined as a period necessary to reach 90% value of ΔEMF_{SG} from the EMF value in a base gas and in a sample gas, respectively.

3. Results and Discussions

3.1. Characterization of metal oxide powders loaded with and without Au nanoparticles

Figure 2 shows XRD spectra of all the MO powders prepared, together with their crystallite size (CS), which was calculated by using Scherrer equation. The XRD spectrum of each the MO powder which was prepared with an $In(NO_3)_3$, $Zn(NO_3)_2$ or $Co(NO_3)_2$ aqueous solution was attributed to a single phase of In_2O_3 (JCPDS No. 01-089-4595), ZnO (JCPDS No. 00-306-1451) or Co_3O_4 (JCPDS No. 00-042-1467), respectively. In addition, the crystallite size which was calculated by using the (222) peak of In_2O_3, the (101) peak of ZnO or the (311) peak was ca. 19.8, 44.0 or 22.7 nm, respectively. Figure 3 shows N_2 adsorption-desorption isotherms and pore-size distributions of all the MO powders, together with their specific surface area (SSA). The N_2 adsorption-desorption isotherms of the In_2O_3 and Co_3O_4 powders belong to "Type IV" according to the BET classification [33], because of abrupt and quite small increase in volume of adsorbed N_2 at low P/P_0 (≤ 0.2), small positive slope of quasi-plateau at a medium P/P_0 (0.2~0.8) range and the abrupt and large increase in volume of adsorbed N_2 and hysteresis at a high P/P_0 values (≥ 0.8) range. The hysteresis behavior is associated with capillary condensation and evaporation of N_2 in and from their mesopores, respectively. However, the amount of N_2 adsorbed on the In_2O_3 powder was much larger than that on the Co_3O_4 powder, and the In_2O_3 powder showed a too large hysteresis loop in comparison with that of the Co_3O_4 powder. On the other hand, the N_2

adsorption-desorption isotherms of the ZnO powder belong to "Type II" [33]. Therefore, the In_2O_3 powder had relatively well-developed mesopores at the pore diameter of several ten nanometers with a large SSA value (ca. 37.6 $m^2 g^{-1}$), while the mesopore volume of the Co_3O_4 powder, which showed relatively a small SSA value (ca. 9.3 $m^2 g^{-1}$), was much smaller than that of the In_2O_3 powder and the ZnO powder had only small pore volume and an extremely small SSA value (ca. 0.8 $m^2 g^{-1}$).

Figure 4 shows TEM images of all *2.0*Au/MO(*400*air) powders. The size of Au nanoparticles loaded on the MO powders was largely dependent on the kind of the MO, even though the Au nanoparticles were loaded on the MO powders at the same conditions. Namely, relatively small and uniform Au nanoparticles were loaded on both the *2.0*Au/In_2O_3(*400*air) and *2.0*Au/ZnO(*400*air) powders in comparison with that of the *2.0*Au/Co_3O_4(*400*air) powder, and the diameter of the Au nanoparticles on the *2.0*Au/In_2O_3(*400*air) or *2.0*Au/ZnO(*400*air) powder was around 5 or 10 nm, respectively. On the other hand, Au nanoparticles in different sizes (several nm in diameter) were loaded on the *2.0*Au/Co_3O_4(*400*air) powder.

Figure 5 shows SEM images of the electrode surface of all EC(MO) and EC(*2.0*Au/MO(*400*air)) sensors, together with their electrode thickness. The ACP was mixed with the MO powders, but the morphology of the MO powders can be easily observed in this images, because of the small amount of the mixed ACP (only 5 wt%). The electrode of the EC(In_2O_3) sensor consists of agglomerated secondary In_2O_3 particles with a size of several micrometers. The geometric surface area (GSA) calculated from the CS (19.8 nm) was ca. 42.2 $m^2 g^{-1}$, assuming the real density of In_2O_3 is 7.18 g cm^{-3} [34] and the morphology of all the crystallites is spherical. Since the GSA value is similar to the SSA value (37.6 $m^2 g^{-1}$), In_2O_3 particles are considered to be almost single crystal and the well-developed mesopores shown in Fig. 3(b)(i) are suggested to be formed in the secondary In_2O_3 particles. The morphology of the most of ZnO particles was hexagonally columnar with smooth surface.

Considering that the particle size calculated from the SSA (0.8 m^2 g^{-1}) and the real density (5.67 g cm^{-3} [34]) is ca. 1.32 μm and the CS estimated by XRD is ca. 44.0 nm, the columnar ZnO particles seem to consist of polycrystals with little mesopores. On the other hand, the Co_3O_4 particles showed plate-like morphology. The particles size of Co_3O_4 calculated from its SSA (9.3 m^2 g^{-1}) and its real density (6.11 g cm^{-3} [34]) is 115 nm and this value is larger than its CS (22.7 nm). This also suggests that Co_3O_4 is polycrystal and is also relatively dense with few mesopores. The morphology of the *2.0*Au/MO(*400*air) powders were almost comparable to that of the MO powders. In addition, all the electrodes have submicron-ordered macropores among the agglomerated secondary particles, and thus the target gas (CO) as well as the base gas (the mixture of O_2 and N_2 containing H_2O) were easily diffused into the electrodes. The electrode thickness was largely dependent on the kind of oxide powders, because it was very difficult to adjust the cohesive properties of the pastes containing the MO or *2.0*Au/MO(*400*air) powder. However, the electrode thickness of all sensors could be controlled between ca. 70 μm and ca. 340 μm, as indicated in Fig. 5.

3.2. Gas-sensing properties of EC(MO) and EC(*2.0*Au/MO(*400*air)) sensors

Figure 6 shows response transients of all EC(MO) sensors, which were both as-fabricated and subsequently stored for 3 weeks in laboratory atmosphere, to 500 ppm CO and 500 ppm H_2 in wet synthetic air at 30ºC (57%RH). The magnitude of response (ΔEMF_{SG}), CO selectivity against H_2 ($\Delta EMF_{CO}/\Delta EMF_{H_2}$) and 90% response and recovery times of the sensors were summarized in Tables 1 and 2. All the as-fabricated EC(MO) sensors showed a negative response to both CO and H_2, and the CO response of all the sensors was a slightly larger than their H_2 responses. Among them, the as-fabricated EC(In_2O_3) and EC(ZnO) sensors showed stable and large responses to both CO and H_2 with relatively slow response and recovery speeds, in comparison with those of the as-fabricated EC(Co_3O_4) sensor. In

addition, the CO selectivity of the as-fabricated EC(ZnO) sensor against H_2 was larger than that of the as-fabricated EC(In_2O_3) sensor. The sensing properties of both the EC(In_2O_3) and EC(ZnO) sensors, which showed relatively-large CO and H_2 responses, were measured again after the 3-week storage from the first measurement. The EMF of both the EC(In_2O_3) and EC(ZnO) sensors in the wet synthetic air shifted negatively after the 3-week storage, and the magnitude of the shifted EMF of the EC(ZnO) sensor (ca. -40 mV) was much larger than that of the EC(In_2O_3) sensor (ca. -8 mV). In addition, the CO response of both the as-fabricated sensors slightly reduced after 3-week storage. The H_2 response of the EC(ZnO) sensor after 3-week storage was comparable to that of the as-fabricated one, while the H_2 response of the EC(In_2O_3) sensor after 3-week storage was much smaller than that of the as-fabricated one. Thus, the CO selectivity of the stored EC(In_2O_3) sensor was larger than that of the stored EC(ZnO) sensor. In addition, the response and recovery speeds of the stored EC(In_2O_3) sensor to both CO and H_2 were much faster than that of the as-fabricated one, and especially the recovery property was largely improved after 3-week storage.

The Au nanoparticles were loaded on all the MO powders, to improve the CO-sensing properties of the EC(MO) sensors. Figure 7 shows response transients of all the as-fabricated and stored EC(*2.0*Au/MO(*400*air)) sensors to 500 ppm CO and 500 ppm H_2 in wet synthetic air at 30ºC (57%RH), but response transient of 3-week stored EC(*2.0*Au/In_2O_3(*400*air)) sensor to 500 ppm H_2 was not measured. The ΔEMF_{SG}, $\Delta EMF_{CO}/\Delta EMF_{H_2}$ and 90% response and recovery times of the sensors were summarized in Tables 1 and 2. The Au loading on the MO surface dramatically enhanced the magnitude of the CO response of both the as-fabricated EC(In_2O_3) and EC(ZnO) sensors, while the as-fabricated EC(*2.0*Au/In_2O_3(*400*air)) sensor showed slight overshooting response behavior to only CO. The response speed of both the as-fabricated EC(In_2O_3) and EC(ZnO) sensors and the recovery speed of the EC(In_2O_3) sensor to CO were also largely improved by the Au loading, while the recovery speed of the

as-fabricated EC(*2.0*Au/ZnO(*400*air)) sensor to CO was comparable to that of the as-fabricated EC(ZnO) sensor. On the other hand, the magnitude of the CO response of the as-fabricated EC(Co_3O_4) sensor was also improved by the Au loading, but the sensor showed extremely slow response speed and therefore quite small CO response even after 60 min exposure to CO, probably because of the extremely slow response speed. The H_2 response of both the as-fabricated EC(In_2O_3) and EC(ZnO) sensors also increased by the 2.0 wt% Au loading, but the CO selectivity against H_2 of the as-fabricated EC(*2.0*Au/In_2O_3(*400*air)) sensor (ca. 2.6) was slightly larger than that of the as-fabricated EC(In_2O_3) sensor (ca. 1.8), while the CO selectivity against H_2 of the as-fabricated EC(*2.0*Au/ZnO(*400*air)) sensor (ca. 2.6) was comparable to that of as-fabricated EC(ZnO) sensor (ca. 2.7). The Au loading also improved the H_2 response of the EC(Co_3O_4) sensor, but the effect was quite small. Thus, the CO selectivity against H_2 of the as-fabricated EC(*2.0*Au/Co_3O_4(*400*air)) sensor (ca. 8.0) was much larger than those of the as-fabricated EC(*2.0*Au/In_2O_3(*400*air)) sensor and as-fabricated EC(*2.0*Au/ZnO(*400*air)) sensor. However, the CO-sensing properties of the stored EC(*2.0*Au/Co_3O_4(*400*air)) sensor were not measured in this study, since the magnitude of CO response and the response and recovery speeds to CO were much poor than we had expected. After 3-week storage, the values of EMF of both the stored EC(*2.0*Au/In_2O_3(*400*air)) and EC(*2.0*Au/ZnO(*400*air)) sensors in wet synthetic air shifted positively and negatively, respectively, in comparison with those of the as-fabricated ones. The magnitude of the shifted EMF of the 3-week stored EC(*2.0*Au/In_2O_3(*400*air)) sensor (ca. 5 mV) was much smaller than that of the 3-week stored EC(*2.0*Au/ZnO(*400*air)) sensor (ca. 22 mV), and it was comparable to that of the 3-week storage EC(In_2O_3) sensor (ca. 8 mV). However, the 8-month storage resulted in a further shift in the EMF of the EC(*2.0*Au/In_2O_3(*400*air)) sensor to a positive direction (ca. +25 mV). On the other hand, the magnitude of the shifted EMF of the 3-week stored EC(*2.0*Au/ZnO(*400*air)) sensor was smaller than that of the 3-week stored EC(ZnO)

sensor. Both the responses to 500 ppm CO and 500 ppm H_2 of the EC(*2.0*Au/In_2O_3(*400*air)) sensor tended to increase with an increase in the storage period, but the 8-month storage hardly improved the CO selectivity against H_2. In addition, the EC(*2.0*Au/In_2O_3(*400*air)) sensor showed relatively fast response speed even after 8-month storage, especially to CO, while the recovery time gradually increased with an increase in the storage period. Totally, the loading of Au nanoparticles on the In_2O_3 drastically enhanced not only the initial CO-sensing properties of the EC(In_2O_3) sensor but also the operation stability after long-term storage. On the other hand, the CO-sensing properties of the EC(*2.0*Au/ZnO(*400*air)) sensor were seriously deteriorated even after 3-week storage. Namely, the long-term stability of the EC(*2.0*Au/ZnO(*400*air)) sensor was found to be much lower than that of the EC(*2.0*Au/In_2O_3(*400*air)) sensor. It is well-known that the catalytic activities of the Au nanoparticles are dramatically dependent on the characteristics of the supports. For example, Ohkuma et al. have reported that ZnO easily reacted with CO_2 in the atmosphere to form carbonate species on the surface [35], and Wang et al. have reported that the catalytic CO-oxidation property of Au-loaded ZnO was reduced by the accumulation of carbonate species to the surface of ZnO [36, 37]. Also in this study, therefore, CO_2, which is generated by the oxidation of CO (target gas) and/or existed in the atmosphere for the 3-week storage, probably adsorbed as carbonate species on the surface of the *2.0*Au/ZnO(*400*air) powder, leading to a reduction in the electrocatalytic activity. In addition, Rodriguez-Gonzalez et al. have demonstrated that the addition of In_2O_3 to Au-loaded TiO_2 effectively improved the long-term stability of the catalytic CO-oxidation activity of the Au-loaded TiO_2 at low temperatures and the behavior is related to the strong anchoring of the Au nanoparticles on the well-dispersed In_2O_3 [38]. Such effectiveness of In_2O_3 may be one of the important factors in maintaining the excellent CO-sensing properties even after 8-month storage.

3.3. Variations in gas-sensing properties of EC(*n*Au/In_2O_3(*400*air)) sensors with the loading amounts of Au

Figure 8 shows concentration dependence of the magnitude of responses to CO and H_2 of EC(*n*Au/In_2O_3(*400*air)) sensors (*n = 0.1*, *0.5*, and *2.0*) in wet synthetic air at 30ºC (57%RH). In addition, the response transients of the EC(*2.0*Au/In_2O_3(*400*air)) sensor as a representative to various concentrations of CO and H_2 are shown in Fig. 9. And their ΔEMF_{SG}, $\Delta EMF_{CO}/\Delta EMF_{H_2}$ and 90% response and recovery times (the concentration of CO and H_2: 500 ppm) were summarized in Tables 1 and 2. The magnitude of responses of all the sensors to CO and H_2 increased in proportion to the logarithm of CO and H_2 concentrations, respectively. The response to low concentration of CO increased with an increase in the loading amount of Au, while the response to high concentration of CO increased only slightly by increasing the loading amount of Au. Thus, the slope of the relationship between the magnitude of the CO response and the logarithm of CO concentration, i.e., the sensitivity, reduced with an increase in the loading amount of Au. In addition, the EC(*2.0*Au/In_2O_3(*400*air)) sensor showed an clear response to even 10 ppm CO with the high signal/noise (S/N) ratio, even though the response and recovery speeds slightly decreased with an decrease in the concentration of CO (see Fig. 9(a)). This means that the large loading amount of Au nanoparticles on the In_2O_3 surface can apparently improve the response to 10 ppm CO. On the other hand, the magnitude of H_2 response of all the EC(*n*Au/In_2O_3(*400*air)) sensors was much smaller than that of their CO response and the H_2 sensitivity tended to increase with an increase in the loading amount of Au, since the responses to lower concentration of H_2 hardly depended on the loading amount of Au and the responses to higher concentration of H_2 increased with an increase in the loading amount of Au. The EC(*0.1*Au/In_2O_3(*400*air)) sensor showed relatively large CO selectivity against H_2 when the concentration of CO and H_2 was 500 ppm, but the response to 10 ppm CO was the smallest

among them. Therefore, the CO-sensing properties of the EC(*2.0*Au/In_2O_3(*400*air)) sensor, which showed the largest response to 10 ppm CO, and the related EC(*2.0*Au/In_2O_3(*T*m)) sensors have been investigated in more detail from the next section.

3.4. Humidity and O_2-concentration dependences of gas-sensing properties of EC(*2.0*Au/In_2O_3(*400*air)) sensor

Effects of humidity and O_2 concentration in the base gas on the CO-sensing properties of the EC(*2.0*Au/In_2O_3(*400*air)) sensor have been investigated. Figure 10 shows response transients of the EC(*2.0*Au/In_2O_3(*400*air)) sensor to 500 ppm CO under dry or wet synthetic air (RH: 0~100%). The CO response of the EC(*2.0*Au/In_2O_3(*400*air)) sensor slightly decreased with a decrease in RH in the range of 40~100%RH, probably because the slight decrease in the OH^- conductivity was caused by the decrease in the amount of moisture in the ACP electrolyte [39]. Further decrease in the amount of moisture in the base gas shifted the EMF value in the base gas negatively and increased the magnitude of overshooting of the CO response with a decrease in RH, and then the EMF drifted largely without a constant tendency under dry atmosphere. Consequently, it was confirmed that the influence in moisture on the CO response was almost negligible in the range of 40~100%RH.

Figure 11 shows O_2 concentration dependence on EMF of the EC(*2.0*Au/In_2O_3(*400*air)) sensor in 500 ppm CO balanced with a mixture of N_2 and O_2 in the SE side at 30ºC (RH: 57%). The EMF shifted positively with an increase in O_2 concentration, and the behavior apparently showed that an electrochemical reaction involving O_2 is one of important factors in detecting CO for this sensor. Miura et al. previously reported that the magnitude of CO response of an electrochemical CO sensor using Nafion as an electrolyte is determined by the mixed potential between CO oxidation and O_2 reduction [40-42]. On the basis of this concept, we have also presumed that the EMF of a potentiometric gas sensor using a pair of Pt-loaded

carbon electrodes and an ACP electrolyte in wet air containing CO [19] is determined by the mixed potential resulting from the following reactions.

$$CO + 2OH^- \rightarrow CO_2 + H_2O + 2e^- \quad (1)$$

$$(1/2)O_2 + H_2O + 2e^- \rightarrow 2OH^- \quad (2)$$

From the results obtained, we are considering that the EMF of the SE of the EC(*2.0*Au/In_2O_3(*400*air)) sensor under wet synthetic air containing CO is also determined by the mixed potential resulting from the above reactions, because the EMF is very sensitive to the change in the concentration of CO as well as O_2.

3.5. Influence of heat-treatment conditions of *2.0*Au/In_2O_3 powders on gas-sensing properties of EC(*2.0*Au/In_2O_3(*T*m)) sensors

The *2.0*Au/In_2O_3 powders was treated at several conditions, and their effects on the response behavior of the EC(*2.0*Au/In_2O_3(*T*m)) sensors to CO and H_2 have been investigated. Figure 12 shows XRD spectra of the *2.0*Au/In_2O_3(*100*air), *2.0*Au/In_2O_3(*400*air), *2.0*Au/In_2O_3(*250*H_2) and *2.0*Au/In_2O_3(*400*H_2) powders. The XRD spectra of *2.0*Au/In_2O_3(*100*air), *2.0*Au/In_2O_3(*400*air) and *2.0*Au/In_2O_3(*250*H_2) powders were attributed to only a single phase of In_2O_3 without any Au peaks, but the XRD spectrum of the *2.0*Au/In_2O_3(*400*H_2) powder consisted of large and small peaks attributed to In metal and $AuIn_2$ alloy, respectively, besides the peaks attributed to the In_2O_3. This result indicates that the In_2O_3 powder was partly reduced at 400°C in H_2. Actually, a lot of spherical metal particles with smooth surface and un-uniform diameter were clearly observed in the SEM image of the *2.0*Au/In_2O_3(*400*H_2) powder, as shown in Fig. 13, whereas the morphology of others (not shown here) was almost identical to that of the *2.0*Au/In_2O_3(*400*air) powder (see Fig. 5(b)). In addition, the CS of In_2O_3 of the *2.0*Au/In_2O_3(*400*H_2) powder, which was calculated by using the (222) peak, ca. 25.8 nm, was slightly larger than that of the pure

In_2O_3 powder (ca. 19.8 nm, see Fig. 2(a)), while those of other *2.0*Au/In_2O_3(*T*m) powders were comparable to that of the pure In_2O_3 powder. The CS of the In metal and $AuIn_2$ alloy contained in the *2.0*Au/In_2O_3(*400*H_2) powder were ca. 41.4 nm and ca. 23.2 nm, respectively, and thus the micron-sized spherical metal particles probably consisted of many In and/or $AuIn_2$ crystallites.

Figure 14 shows TEM images of *2.0*Au/In_2O_3(*100*air) and *2.0*Au/In_2O_3(*250*H_2) powders. Au nanoparticles were not confirmed on the surface of the *2.0*Au/In_2O_3(*100*air) powder at a low magnification (Fig. 14(a)(i)), but many black-shadow spots with a diameter of less than 1 nm (some of them were indicated by arrows) were observed in the high-resolutional TEM image (Fig. 14(a)(ii)). It is highly possible that they may be Au clusters highly-dispersed on the In_2O_3, because the *2.0*Au/In_2O_3(*100*air) powder was merely heat-treated at low temperature (100ºC) in air after the deposition of $Au(OH)_3$. On the other hand, some Au nanoparticles were clearly observed on the surface of the *2.0*Au/In_2O_3(*250*H_2) powder, and the particle size was slightly larger than that of *2.0*Au/In_2O_3(*400*air) powder (see Fig. 4(a)). This result indicates that the heat-treatment under H_2 atmosphere slightly promoted the sintering of Au nanoparticles on the In_2O_3 in comparison with the heat-treatment under air atmosphere. However, Au nanoparticles on the *2.0*Au/In_2O_3(*250*H_2) powder were small enough and well-dispersed with uniform size as in the case of the *2.0*Au/In_2O_3(*400*air) powder.

Figure 15 shows response transients of the as-fabricated EC(*2.0*Au/In_2O_3(*T*m)) sensors to 500 ppm CO and H_2 in wet synthetic air at 30ºC (57%RH). And their ΔEMF_{SG}, $\Delta EMF_{CO}/\Delta EMF_{H_2}$ and 90% response and recovery times were summarized in Table 1 and 2. Most of the sensors showed large response to 500 ppm CO and H_2 to the negative EMF direction, but the as-fabricated EC(*2.0*Au/In_2O_3(*400*H_2)) sensor only showed quite small CO response (thus, the H_2 response and variations in the CO and H_2 responses with the

concentration was not measured in this study). The reduction of In_2O_3 to the In metal and $AuIn_2$ alloy (see Fig. 12(d)) by the heat treatment under H_2 atmosphere at 400ºC might deactivate the electrocatalytic activity of the *2.0*Au/In_2O_3 powder and thus extremely deteriorated the CO-sensing properties. The magnitude of both the CO and H_2 responses of other as-fabricated EC(*2.0*Au/In_2O_3(*T*H_2)) sensors decreased with an increase in the heat-treatment temperature. The In metal or $AuIn_2$ alloy was not observed in the XRD spectra of the *2.0*Au/In_2O_3(*250*H_2) and *2.0*Au/In_2O_3(*100*H_2) powders, but a part of the In_2O_3 surface might be moderately reduced even by the heat treatment under H_2 atmosphere at low temperatures. However, the heat treatment under H_2 atmosphere at moderate temperatures drastically improved the CO selectivity against H_2. Especially, the as-fabricated EC(*2.0*Au/In_2O_3(*250*H_2)) sensor showed relatively large CO response (ca. 65 mV), quite small H_2 response (ca. 2.3 mV), and the largest CO selectivity against H_2 (ca. 28.3) among all the as-fabricated EC(*2.0*Au/In_2O_3(*T*m)) sensors. In addition, the response speed of the as-fabricated EC(*2.0*Au/In_2O_3(*250*H_2)) sensor to both CO and H_2 was comparable to that of other as-fabricated EC(*2.0*Au/In_2O_3(*T*m)) sensors, while the recovery speed of the as-fabricated EC(*2.0*Au/In_2O_3(*250*H_2)) sensor to CO and H_2 was much faster than those of other as-fabricated EC(*2.0*Au/In_2O_3(*T*m)) sensors. On the other hand, the heat treatment of the *2.0*Au/In_2O_3 powder in

air was not effective for improving the magnitude of the response to both 500 ppm CO and H_2, and thus the CO selectivity against H_2 of all the as-fabricated EC(*2.0*Au/In_2O_3(*T*air)) sensors was quite small, compared with that of the as-fabricated EC(*2.0*Au/In_2O_3(*250*H_2)) sensor.

Figure 16 shows CO and H_2 concentration dependences of the responses of the as-fabricated EC(*2.0*Au/In_2O_3(*T*m)) sensors except for the EC(*2.0*Au/In_2O_3(*400*H_2)) sensor. As for the as-fabricated EC(*2.0*Au/In_2O_3(*T*air)) sensors, the CO responses in the low

concentration range (especially 10~500 ppm) increased with an increase in the heat-treatment temperature and the difference in the CO responses originating from the change in the heat-treatment temperature decreased with an increase in the concentration of CO. Thus, the CO sensitivity increased with a decrease in the heat-treatment temperature and the CO responses to high concentration (3000 ppm) decrease with an increase in the heat-treatment temperature. On the other hand, the H_2 responses of the as-fabricated EC(*2.0*Au/In_2O_3(*T*air)) sensors were hardly dependent on the heat-treatment temperature. When the *2.0*Au/In_2O_3 powder was heat-treated under H_2 atmosphere, the CO response of the as-fabricated EC(*2.0*Au/In_2O_3(*T*H_2)) sensors decreased in all the concentration range with an increase in the heat-treatment temperature, and thus the CO sensitivity was hardly dependent on the heat-treatment temperature. However, the as-fabricated EC(*2.0*Au/In_2O_3(*250*H_2)) sensor showed almost no response to H_2 in the range of 10~3000 ppm, while the as-fabricated EC(*2.0*Au/In_2O_3(*100*H_2)) sensor showed relatively large H_2 response, which was comparable to that of the as-fabricated EC(*2.0*Au/In_2O_3(*T*air)) sensors. Thus, the CO selectivity against H_2 of the as-fabricated EC(*2.0*Au/In_2O_3(*250*H_2)) sensor was the largest among all the sensors. The CO response of the as-fabricated EC(*2.0*Au/In_2O_3(*250*H_2)) sensor was the smallest among these sensors, but the sensor showed a clear response (ca. 10 mV) even to 10 ppm CO.

Figure 17 shows the response transients of the as-fabricated and 2-month stored EC(*2.0*Au/In_2O_3(*250*H_2)) sensor to 500 ppm CO and 500 ppm H_2 in wet synthetic air at 30ºC (57%RH). Figure 18 shows CO and H_2 concentration dependence of the responses of the as-fabricated and 2-month stored EC(*2.0*Au/In_2O_3(*250*H_2)) sensors, together with that of the as-fabricated EC(*2.0*Au/In_2O_3(*250*air)) sensor for a comparative purpose. The ΔEMF_{SG}, $\Delta EMF_{CO}/\Delta EMF_{H_2}$ and 90% response and recovery times of these sensors were summarized in Tables 1 and 2. The responses to both CO and H_2 of the stored EC(*2.0*Au/In_2O_3(*250*H_2)) sensor were obviously larger than those of the as-fabricated one in all concentration range,

and the enhancement in the H_2 response by the 2-month storage was much larger than that in the CO response. Therefore, the CO selectivity against H_2 of the as-fabricated EC(*2.0*Au/In_2O_3(*250*H_2)) sensor drastically reduced after the 2-month storage. In addition, the concentration dependence of both CO and H_2 responses of the stored EC(*2.0*Au/In_2O_3(*250*H_2)) sensor gradually got close to that of both CO and H_2 responses of the as-fabricated EC(*2.0*Au/In_2O_3(*250*air)) sensor after the 2-month storage. The change in the sensing properties of the EC(*2.0*Au/In_2O_3(*250*H_2)) sensor to both CO and H_2 with the storage period may result from the surface oxidation of In_2O_3 and/or Au nanoparticles by O_2 in the atmosphere. Therefore, the compositional and morphological changes in the surface and bulk of In_2O_3 and Au nanoparticles with treatments under various gaseous conditions at different temperatures are presently being investigated to understand the CO and H_2 sensing mechanism accurately.

4. Conclusions

The EC(MO) and EC(*n*Au/MO(*T*m)) sensors were fabricated and their CO-sensing properties were investigated. All sensors showed negative response to both CO and H_2 in wet synthetic air at 30ºC (RH: 57%), and the CO response of all the sensors was larger than their H_2 response. The Au loading to metal oxides dramatically improved the CO responses. The EC(*2.0*Au/In_2O_3(*400*air)) sensor showed the largest and fastest CO response with relatively high CO selectivity against H_2 and an excellent long-term stability among the EC(*n*Au/MO(*400*air)) sensors. In addition, the magnitude of responses to both CO and H_2 of the EC(*2.0*Au/In_2O_3(*400*air)) sensor increased in proportion to the logarithm of CO and H_2 concentrations, respectively, and the sensor showed relatively large response to CO as low as 10 ppm (ca. 40 mV). The magnitude of the CO response of the EC(*2.0*Au/In_2O_3(*400*air)) sensor largely depended on the humidity, but the influence was almost negligible in the

relative humidity range of 40~100%RH. In addition, the EMF of the EC(*2.0*Au/In_2O_3(*400*air)) sensor to 500 ppm CO in a mixture of wet N_2 and O_2 was dependent on the O_2 concentration, and thus the EMF of the sensor was considered to be determined by the mixed potential between CO oxidation and O_2 reduction. The heat-treatment conditions of the *2*Au/In_2O_3 powder also largely influenced the CO-sensing properties of the EC(*2.0*Au/In_2O_3(*T*m)) sensors. Especially, the as-fabricated EC(*2.0*Au/In_2O_3(*250*H_2)) sensor showed excellent CO selectivity against H_2 in their concentration range of 10~3000 ppm, and the CO-sensing properties of the sensor were the most excellent among the electrochemical CO sensors operable at RT, which were reported previously.

References

1. D. W. Seo, M. A. Hossain, D. H. Lee, Y. D. Lim, S. H. Lee, H. C. Lee, T. W. Hong, W. G. Kim, Electrochim. Acta, 86 (2012) 360-365.
2. X. Ren, S. C. Price, A. C. Fackson, N. Pomerantz, F. L. Beyer, ACS Appl. Mater. Inter., 6 (2014) 13330-13333.
3. N. Li, Y. Leng, M. A. Hickner, C.-Y. Wang, J. Am. Chem. Soc., 135 (2013) 10124-10133.
4. X. Li, Y. Yu, Q. Liu, Y. Meng, J. Membr. Sci., 436 (2013) 202-212.
5. Y.-C. Cao, X. Wang, K. Scott, J. Power Sources, 201 (2012) 226-230.
6. K. Matsumoto, T. Fujigaya, H. Yanagi, N. Nakashima, Adv. Funct. Mater., 21 (2011) 1089-1094.
7. N. Miura, H. Yamazoe, T. Seiyama, Denki Kagaku (presently Electrochemistry), 50 (1982) 858-859.
8. N. Miura, H. Kato, N. Yamazoe, T. Seiyama, Proc. of Intern. Meeting on Chem. Sens., Fukuoka, Japan (1983) pp. 233-238.
9. Y. Gao, H. Kita, Y. Watanabe, K. Sima, J. Appl. Electrochem., 23 (1993) 1102-1106.
10. H. Yan, C.-C. Liu, Sens. Actuators B, 17 (1994) 165-168.
11. P. D. van der Wal, N. F. de Rooij, M. Koudelka-Hep, Sens. Actuators B, 35-36 (1996) 119-123.
12. K. Wallgren, S. Sotiropoulos, Electrochim. Acta, 46 (2001) 1523-1532.
13. S. Stegmeier, M. Fleischer, A. Tawil, P. Hauptmann, K. Egly, K. Rose, Procedia Chem., 1 (2009) 236-239.
14. S. Stegmeier, M. Fleischer, A. Tawil, P. Hauptmann, K. Egly, K. Rose, Sens. Actuators B, 154 (2011) 270-276.
15. M. Manoukian, A. B. LaConti, L. A. Tempelman, J. Forchione, U.S. Patent 2011/0005928 (2011).

16. T. Hyodo, C. Ishibashi, K. Matsuo, K. Kaneyasu, H. Yanagi, Y. Shimizu, Electrochim. Acta 82 (2012) 19-25.
17. T. Hyodo, C. Ishibashi, H. Yanagi, K. Kaneyasu, Y. Shimizu, Reports of the Faculty of Engineering, Nagasaki University, 42(79) (2012) 42-47.
18. T. Goto, T. Hyodo, K. Kaneyasu, H. Yanagi, Y. Shimizu, ECS Trans., 50(12) (2013) 267-272.
19. T. Goto, T. Hyodo, K. Kaneyasu, Y. Shimizu, Chemical Sensors, 29 (2013) 94-96.
20. R. Sorita, T. Kawano, Sens. Actuators B, 40 (1997) 29-32.
21. N. Miura, T. Raisen, G. Lu, N. Yamazoe, Sen. Actuators B, 47 (1998) 84-91.
22. H. Takeda, T. Hyodo, Y. Shimizu, Chemical Sensors B, 29 (2013) 82-84.
23. H. Takeda, T. Ueda, K. Kamada, K. Matsuo, T. Hyodo, Y. Shimizu, Electrochim. Acta, 155 (2015) 8-15.
24. I. J. Kim, S. D. Han, I. Singh, H. D. Lee, J. S. Wang, Sens. Actuators B, 107 (2005) 825-830.
25. J. Su, X.-X. Zou, Y.-C. Zou, G.-D. Li, P.-P. Wang, J.-S. Chen, Inorg. Chem., 52 (2013) 5924-5930.
26. M. Hjiri, R. Dhahri, K. Omri, L. E. Mir, S. G. Leonardi, N. Donato, G. Neri, Mater. Sci. Semicond. Process., 27 (2014) 319-325.
27. J. H. Yu, G. M. Choi, J. Electroceram., 8 (2002) 249-255.
28. Q. Hu, S. Liu, Y. Lian, Phys. Status Solidi A, 211 (2014) 2729-2734.
29. M. Haruta, S. Tsubota, T. Kobayashi, H. Kageyama, M. J. Genet, B. Delmon, J. Catal., 114 (1993) 175-192.
30. M. Daté, Y. Ichihashi, T. Yamashita, A. Chiorino, F. Boccuzzi, M. Haruta, Catal. Today, 72 (2002) 89-94.
31. L.-F. Gutierrez, S. Hamoudi, K. Belkacemi, *Catalysts*, 1 (2011) 97-154.

32. J. C. Y. Kah, N. Phonthammachai, R. C. Y. Wan, J. Song, T. White, S. Mhaisalkar, I. Ahmad, C. Sheppard, M. Olivo, Gold Bull., 41 (2008) 23-36.
33. K. S. W. Sing, Pure Appl. Chem., 54 (1982) 2201-2218.
34. M. J. O'Neil (Ed.), The Merck Index, 14th ed., Merck & Co., Inc., 2006.
35. N. Ohkuma, Y. Funayama, H. Ito, N. Mizutani, M. Kato, J. Surf. Sci. Soc. Jpn, 9-6 (1998) 42-48.
36. G. Wang, W. Zhang, H. Lian, Q. Liu, D. Jiang, T. Wu, React. Kinet. Catal. Lett., 75-2 (2002) 343-351.
37. G.Y. Wang, W. X. Zhang, H. L. Lian, D. Z. Jiang, T. H. Wu, Appl. Catal. A, 239 (2003) 1-10.
38. V. Rodriques-Gonzalez, R. Zanella, L. A. Calzada, R. Gomez, J. Phys. Chem. C, 113 (2009) 8911-8917.
39. D. Stoica, F. Alloin, S. Marais, D. Langevin, C. Chappey, P. Judeinstein, J. Phys. Chem. B, 112 (2008) 12338‑12346.
40. N. Miura, H. Kato, N. Yamazoe, T. Seiyama, Denki Kagaku (presently Electrochemistry), 50 (1982) 858.
41. N. Miura, H. Kato, N. Yamazoe, T. Seiyama, Proc. of Intern. Meeting on Chem. Sens., Fukuoka, Japan, (1983) 233.
42. N. Miura, K. Kanamaru, Y, Shimizu, N. Yamazoe, Solid State Ionics, 40-41 (1990) 452-455.

Figure Captions

Fig. 1. Schematic drawings of (a) sensor element and (b) a gas-sensing measurement system with two electrode compartments.

Fig. 2. XRD spectra of all the MO powders, together with their crystallite sizes (CS).

Fig. 3. (a) N_2 adsorption-desorption isotherms with specific surface area (SSA) and (b) pore-size distributions of all the MO powders.

Fig. 4. TEM images of *2.0*Au/MO(*400*air) powders. Representative Au nanoparticles were marked by arrowheads.

Fig. 5. SEM images of the electrode surface of EC(MO) and EC(*2.0*Au/MO(*400*air)) sensors, together with their electrode thickness.

Fig. 6. Response transients of EC(MO) to 500 ppm CO and 500 ppm H_2 in wet synthetic air at 30ºC (57%RH).

Fig. 7. Response transients of EC(*2.0*Au/MO(*400*air)) to 500 ppm CO and 500 ppm H_2 in wet synthetic air at 30ºC (57%RH).

Fig. 8. CO and H_2 concentration dependence of the responses of EC(*n*Au/In_2O_3(*400*air)) (n: *0.1*, *0.5* or *2.0*) in wet synthetic air at 30ºC (57%RH).

Fig. 9. Response transients of EC(*2.0*Au/In_2O_3(*400*air)) to various concentrations of (a) CO and (b) H_2 in wet synthetic air at 30ºC (57%RH).

Fig. 10. Response transients of EC(*2.0*Au/In_2O_3(*400*air)) to 500 ppm CO under various RH in synthetic air at 30ºC.

Fig. 11. O_2 concentration dependence of EMF of EC(*2.0*Au/In_2O_3(*400*air)) in 500 ppm CO balanced with a mixture of wet N_2 and O_2 at 30ºC (57%RH). O_2 concentration of the SE side was changed in the range of 10~40%, and then O_2 concentration of the CE side was kept constant at 20%.

Fig. 12. XRD spectra of *2.0*Au/In_2O_3(*T*m) powders treated at several conditions, together

with the crystallite size of In, In_2O_3 and $AuIn_2$.

Fig. 13. SEM image of the *2.0*Au/In_2O_3(*400*H_2) powder. Representative In metal or $AuIn_2$ alloy particles were marked by arrowheads.

Fig. 14. TEM images of (a) *2.0*Au/In_2O_3(*100*air) and (b) *2.0*Au/In_2O_3(*250*H_2) powder. The representative Au nanoparticles were marked by arrowheads.

Fig. 15. Response transients to 500 ppm (a) CO and (b) H_2 of EC(*2.0*Au/In_2O_3(*T*m)) in wet synthetic air at 30ºC (57%RH).

Fig. 16. CO and H_2 concentration dependence of the responses of EC(*2.0*Au/In_2O_3(*T*m)) sensors in wet synthetic air at 30ºC (57%RH).

Fig. 17. Response transients of as-fabricated and 2-month stored EC(*2.0*Au/In_2O_3(*250*H_2)) sensor to 500 ppm CO and 500 ppm H_2 in wet synthetic air at 30ºC (57%RH).

Fig. 18. CO and H_2 concentration dependence of the responses of as-fabricated and 2-month stored EC(*2.0*Au/In_2O_3(*250*H_2)) sensor in wet synthetic air at 30ºC (57%RH), together with those of the as-fabricated EC(*2.0*Au/In_2O_3(*250*air)) sensor.

Table 1. Responses to 500 ppm CO and H_2 of all the sensors, together with CO selectivity against H_2.

Sensors	As-fabricated			3-week stored		
	ΔEMF_{SG} / mV		$\Delta EMF_{CO}/\Delta EMF_{H_2}$	ΔEMF_{SG} / mV		$\Delta EMF_{CO}/\Delta EMF_{H_2}$
	CO	H_2		CO	H_2	
EC(ZnO)	32.0	12.0	2.7	28.0	12.0	2.3
EC(*2.0*Au/ZnO(*400*air))	70.0	27.0	2.6	29.0	11.0	1.9
EC(Co_3O_4)	1.8	0.5	3.6	-	-	-
EC(*2.0*Au/Co_3O_4(*400*air))	17.5	2.2	8.0	-	-	-
EC(In_2O_3)	15.5	7.4	1.8	10.5	2.6	4.0
EC(*0.1*Au/In_2O_3(*400*air))	65.0	4.5	14.4	-	-	-
EC(*0.5*Au/In_2O_3(*400*air))	85.0	23.0	3.7	-	-	-
EC(*2.0*Au/In_2O_3(*400*air))	90.0	35.0	2.6	97.0 (120.0*)	- (52.0*)	- (2.3*)
EC(*2.0*Au/In_2O_3(*400*H_2))	4.3	-	-	-	-	-
EC(*2.0*Au/In_2O_3(*250*air))	100.0	34.0	2.9	-	-	-
EC(*2.0*Au/In_2O_3(*250*H_2))	65.0	2.3	28.3	74.0**	23.0**	3.2**
EC(*2.0*Au/In_2O_3(*100*air))	90.0	41.0	2.2	-	-	-
EC(*2.0*Au/In_2O_3(*100*H_2))	100.0	33.0	3.0	-	-	-

*: After 8-month storage, **: after 2-month storage.

Table 2. 90% response and recovery times of all the sensors.

Sensors	As-fabricated				3-week stored			
	500 ppm CO		500 ppm H_2		500 ppm CO		500 ppm H_2	
	Res. / min	Rec. / min	Res. / min	Rec. / min	Res. / min	Rec. / min	Res. / min	Rec. / min
EC(ZnO)	5.0	15.0	22.0	20.0	11.0	6.0	11.0	24.0*
EC(*2.0*Au/ZnO(*400*air))	2.5	14.0	12.0	25.0	20.0	53.0	26.0	46.0 (22.0*)
EC(Co_3O_4)	0.3	0.3	0.3	0.2	-	-	-	-
EC(*2.0*Au/ Co_3O_4(*400*air))	43.0	55.0*	0.2	0.2	-	-	-	-
EC(In_2O_3)	12.0	28.0	14.0	22.0	7.0	1.0	3.0	3.0
EC(*0.1*Au/In_2O_3(*400*air))	1.0	9.5	18.0	30.0	-	-	-	
EC(*0.5*Au/In_2O_3(*400*air))	0.2	4.0	5.8	18.0	-	-	-	
EC(*2.0*Au/In_2O_3(*400*air))	0.1	5.0	5.0	29.0	0.5 (0.5**)	11.0 (24.0**)	- (7.0**)	- (36.0**)
EC(*2.0*Au/In_2O_3(*400*H_2))	2.5	2.0	-	-	-	-	-	-
EC(*2.0*Au/In_2O_3(*250*air))	0.2	11.0	10.0	38.0	-	-	-	-
EC(*2.0*Au/In_2O_3(*250*H_2))	0.5	2.0	10.0	10.0	1.0***	17.0***	38.0***	12.0***
EC(*2.0*Au/In_2O_3(*100*air))	1.5	23.0	7.0	31.0	-	-	-	-
EC(*2.0*Au/In_2O_3(*100*H_2))	0.2	16.5	9.0	35.0	-	-	-	-

*: 60% recovery time, **: after 8-month storage, ***: after 2-month storage.

(a) Sensor structure (an electrochemical cell)

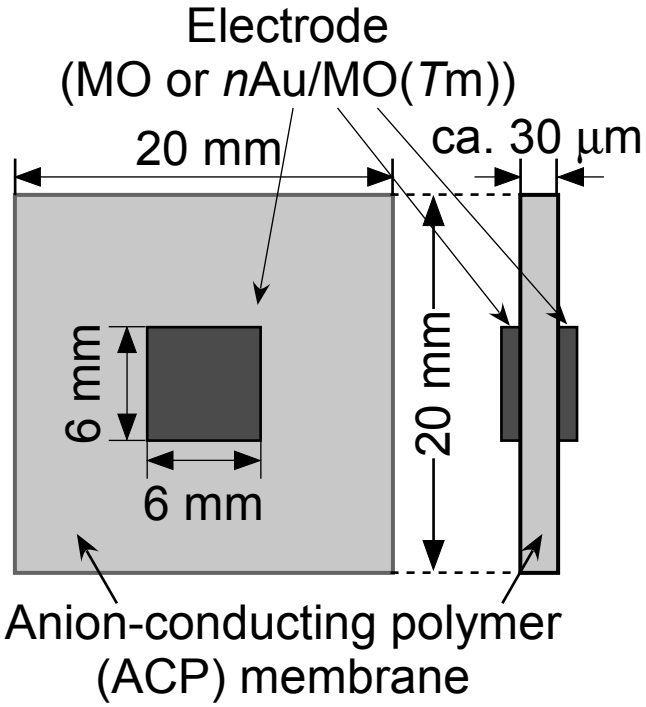

(b) Gas-sensing measurement system

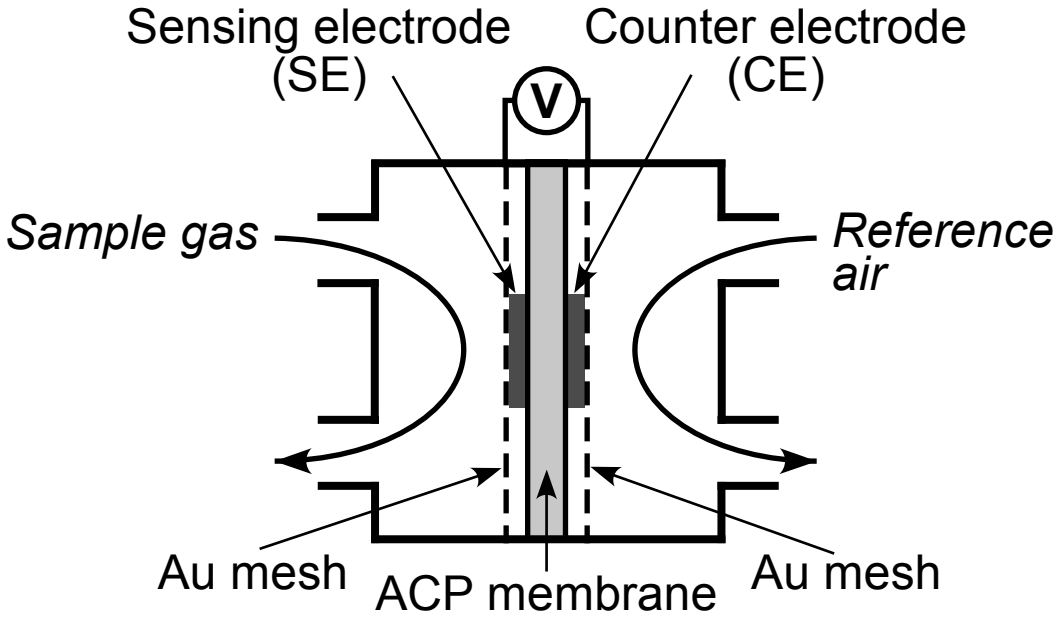

Figure 1. Schematic drawings of (a) sensor structure and (b) a gas-sensing measurement system with two electrode compartments.

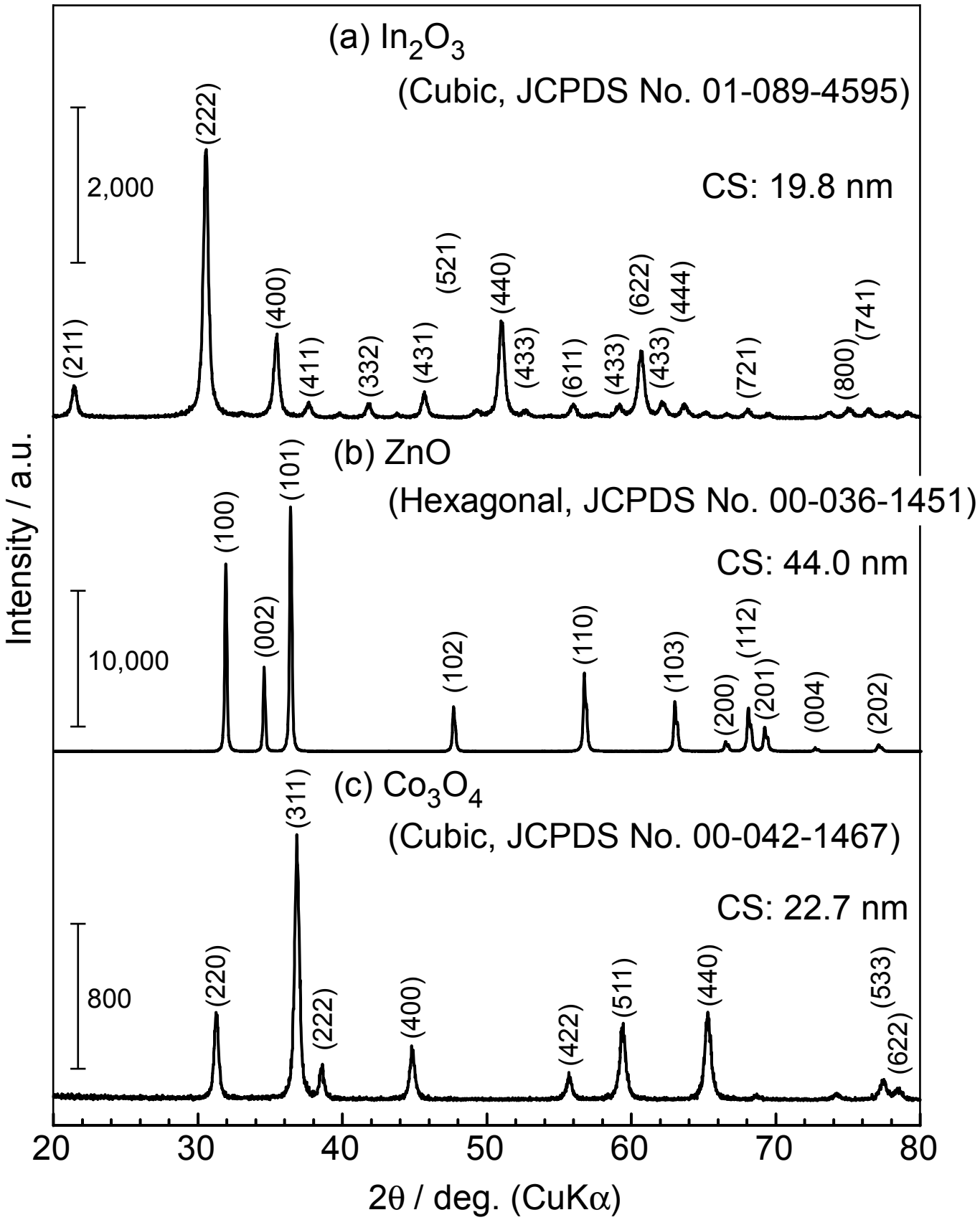

Figure 2. XRD spectra of all MO powders, together with their crystallite sizes (CS).

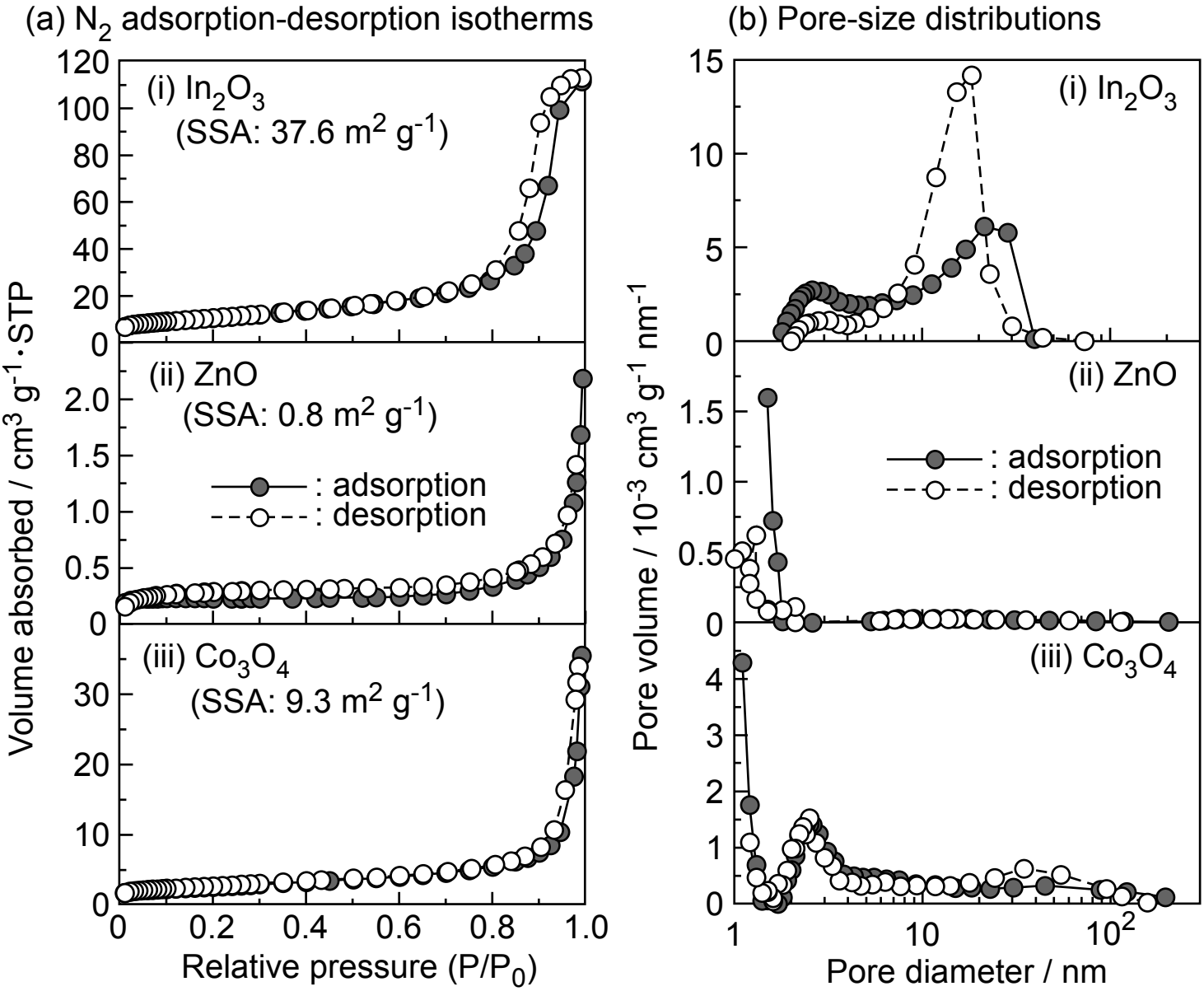

Figure 3. (a) N_2 adsorption-desorption isotherms with specific surface area (SSA) and (b) pore-size distributions of all MO powders.

(a) *2.0*Au/In_2O_3(*400*air) powder

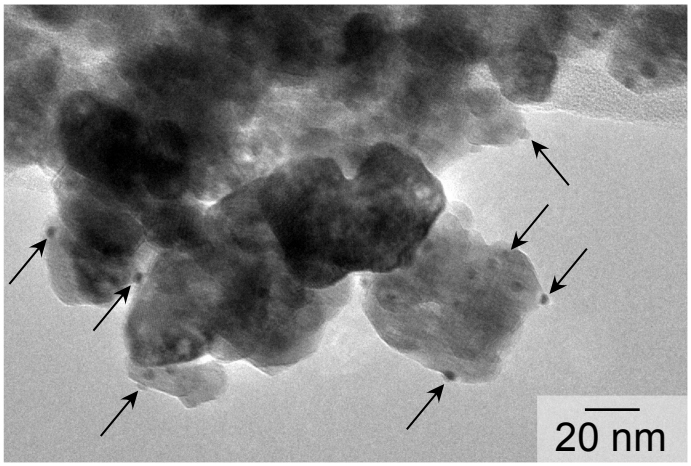

(b) *2.0*Au/ZnO(*400*air) powder

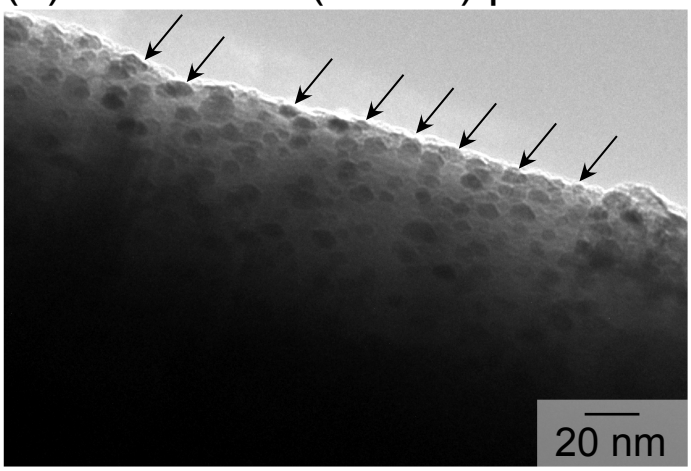

(c) *2.0*Au/Co_3O_4(*400*air) powder

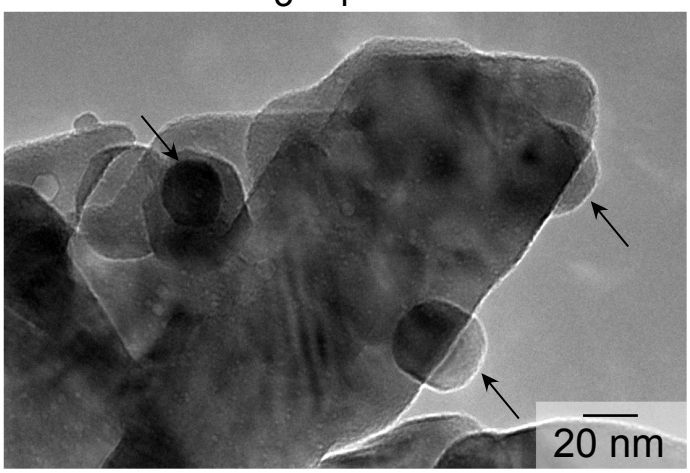

Figure 4. TEM images of *2.0*Au/MO(*400*air) powders. Representative Au nanoparticles were marked by arrowheads.

(a) EC(In_2O_3)

Electrode thickness: ca. 221 μm

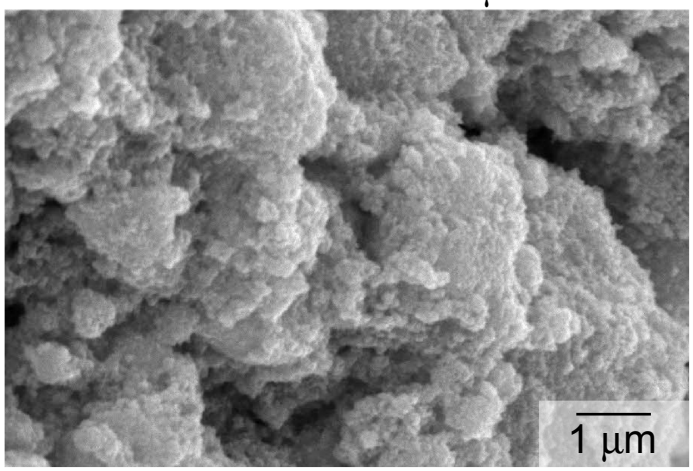

(b) EC(*2.0*Au/In_2O_3(*400*air))

Electrode thickness: ca. 71 μm

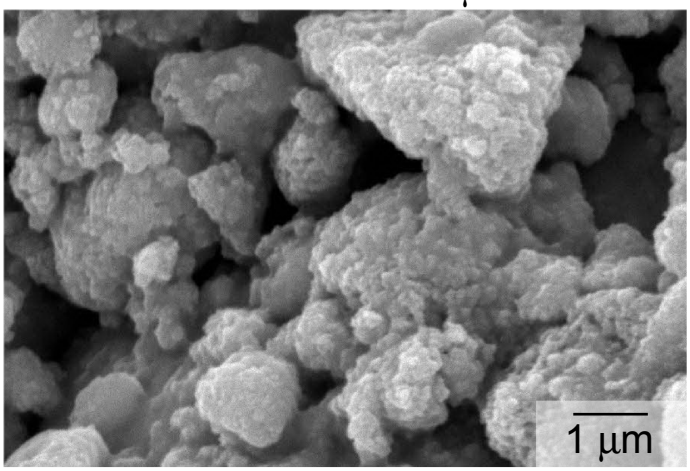

(c) EC(ZnO)

Electrode thickness: ca. 188 μm

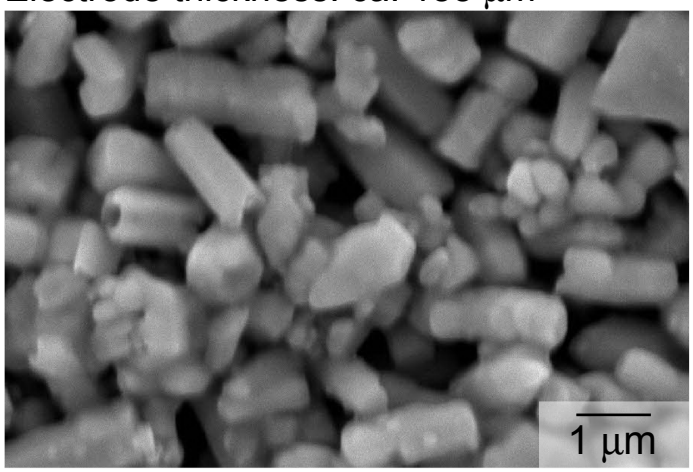

(d) EC(*2.0*Au/ZnO(*400*air))

Electrode thickness: ca. 162 μm

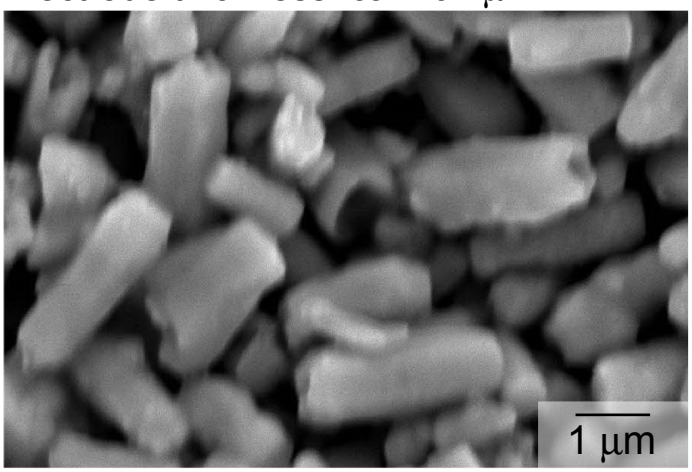

(e) EC(Co_3O_4)

Electrode thickness: ca. 143 μm

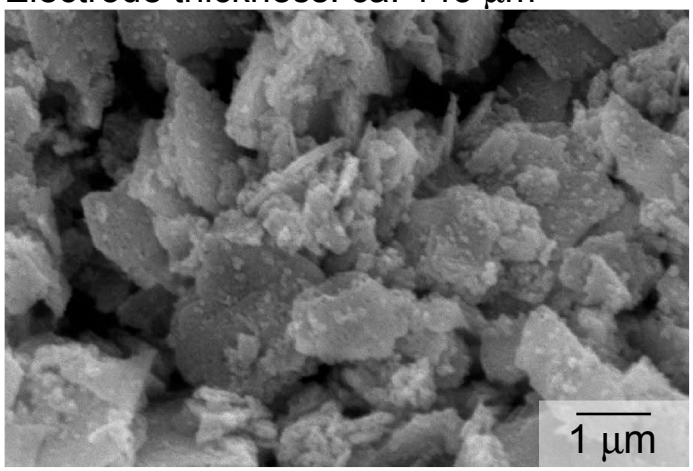

(f) EC(*2.0*Au/Co_3O_4(*400*air))

Electrode thickness: ca. 333 μm

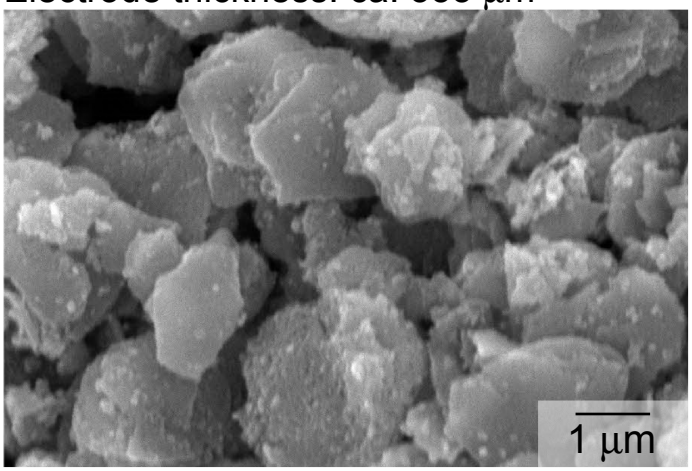

Figure 5. SEM images of the electrode surface of EC(MO) and EC(*2.0*Au/MO(*400*air)) sensors, together with their electrode thickness.

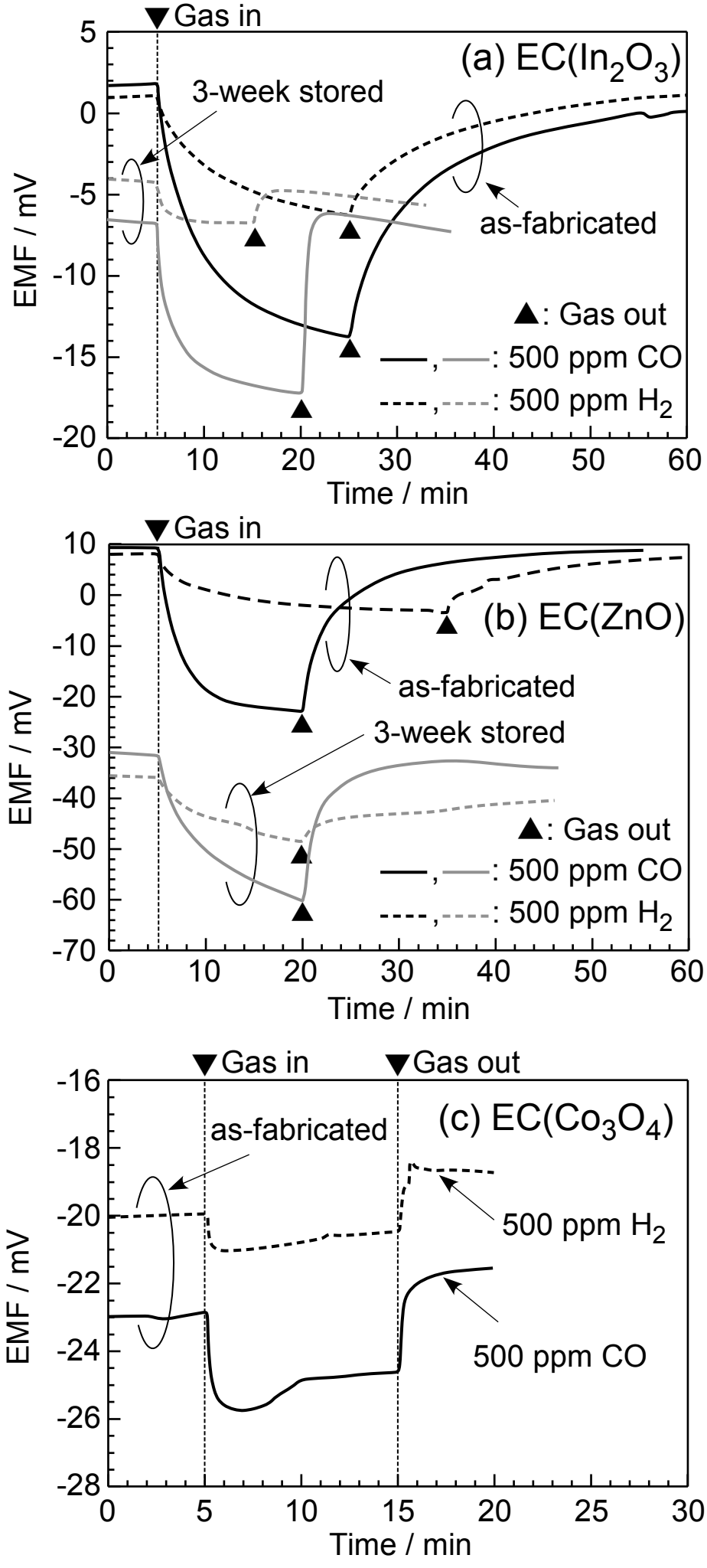

Figure 6. Response transients of EC(MO) to 500 ppm CO and 500 ppm H_2 in wet synthetic air at 30°C (57%RH).

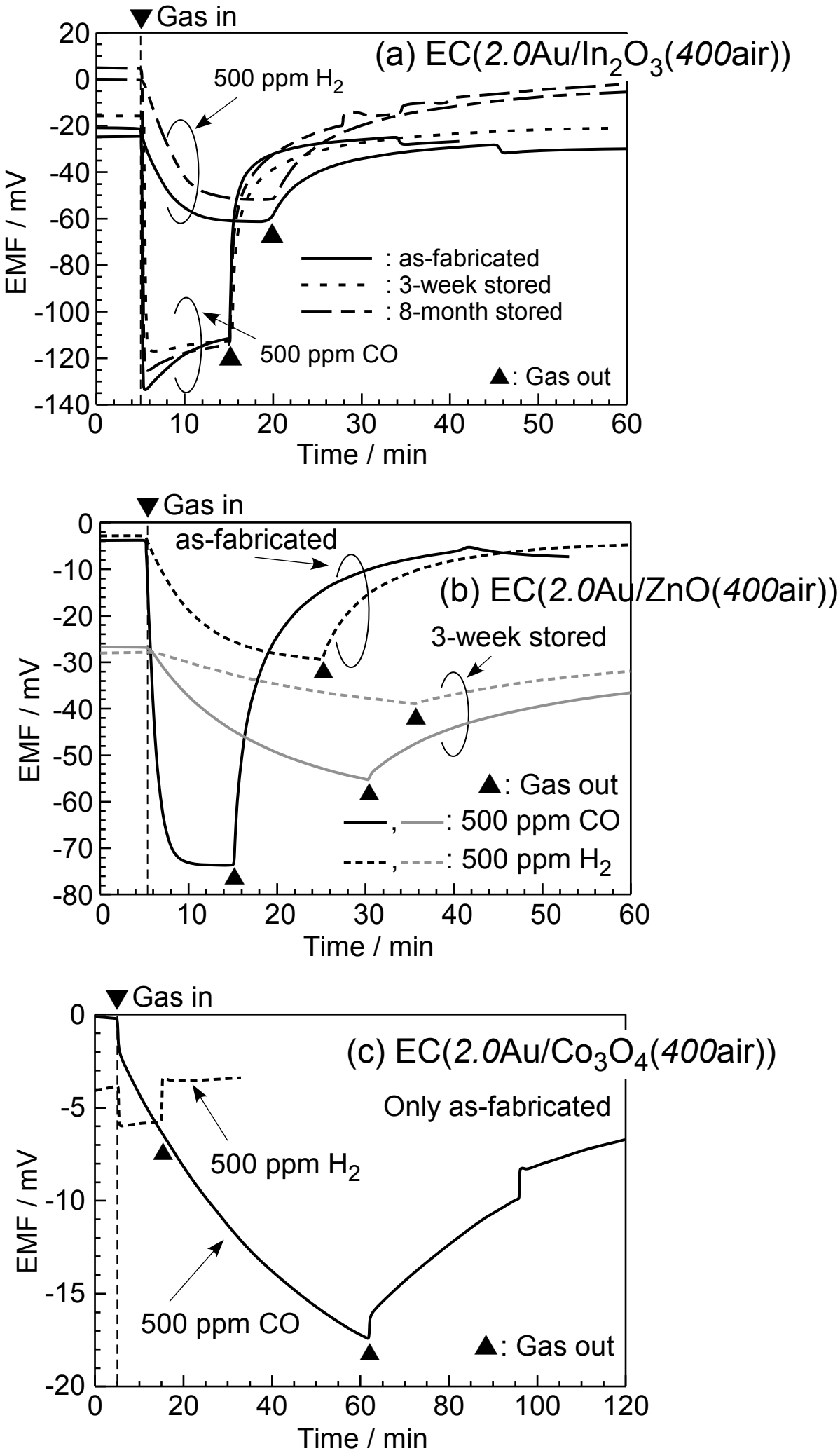

Figure 7. Response transients of EC(*2.0*Au/MO(*400*air)) to 500 ppm CO and 500 ppm H_2 in wet synthetic air at 30°C (57%RH).

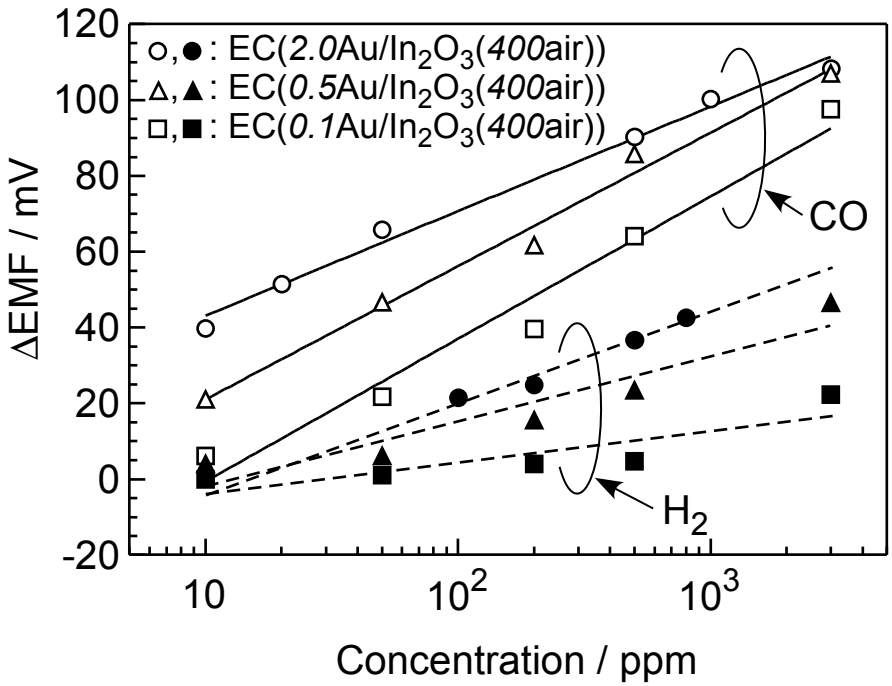

Figure 8. CO and H_2 concentration dependence of the responses of EC(*n*Au/In_2O_3(*400*air)) (*n*: *0.1*, *0.5* or *2.0*) in wet synthetic air at 30°C (57%RH).

(a) CO response

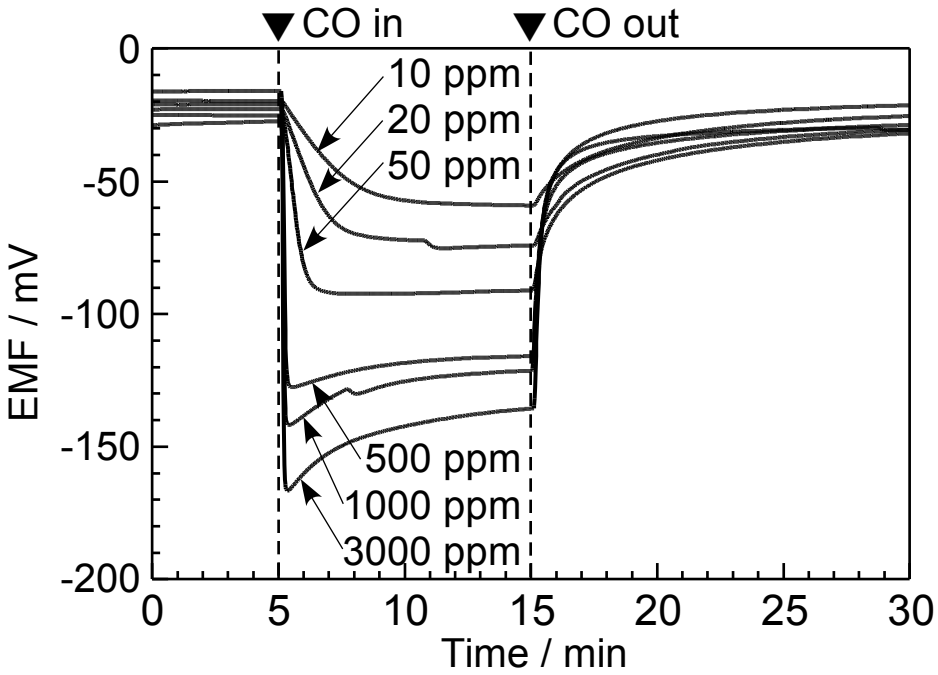

(b) H_2 response

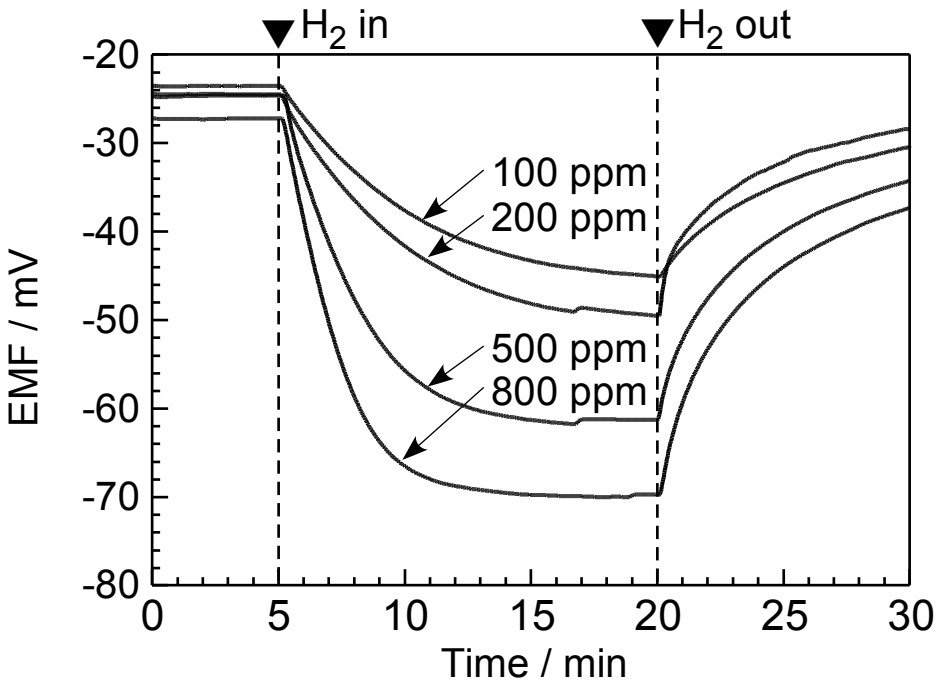

Figure 9. Response transients of EC(*2.0*Au/In_2O_3(*400*air)) to various concentrations of (a) CO and (b) H_2 in wet synthetic air at 30°C (57%RH).

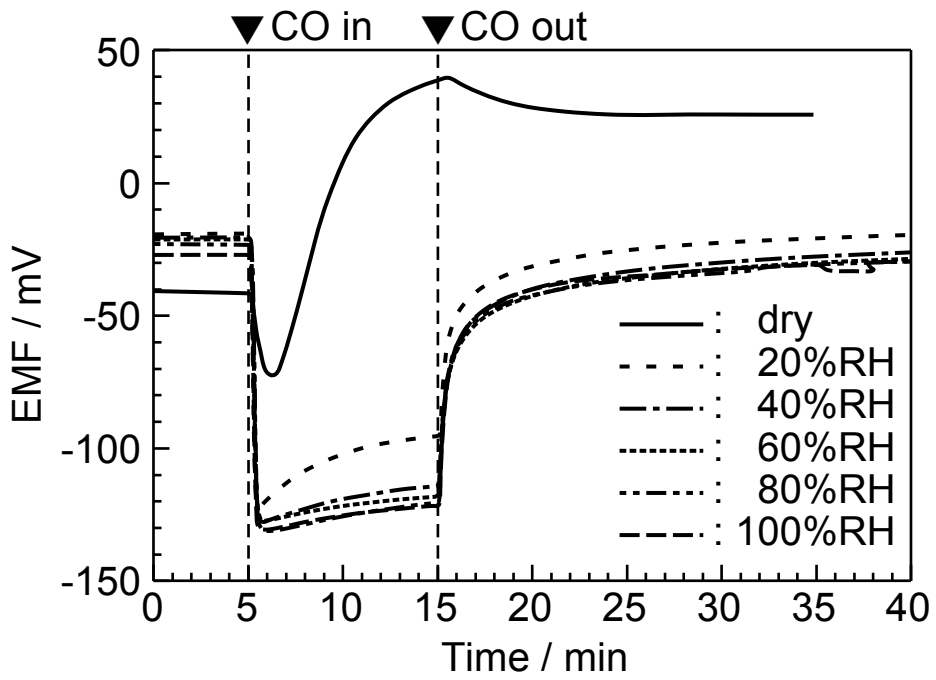

Figure 10. Response transients of EC(*2.0*Au/In_2O_3(*400*air)) to 500 ppm CO under various RH in synthetic air at 30°C.

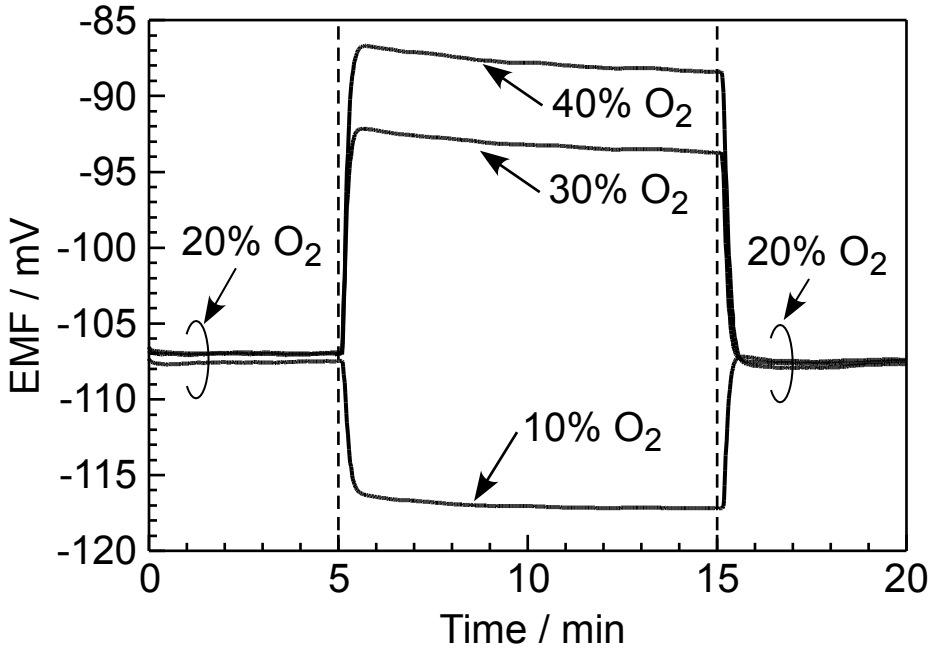

Figure 11. O_2 concentration dependence of EMF of EC(*2.0*Au/In_2O_3(*400*air)) in 500 ppm CO balanced with a mixture of wet N_2 and O_2 at 30°C (57%RH). O_2 concentration of the SE side was changed in the range of 10~40%, and then O_2 concentration of the CE side was kept constant at 20%.

the

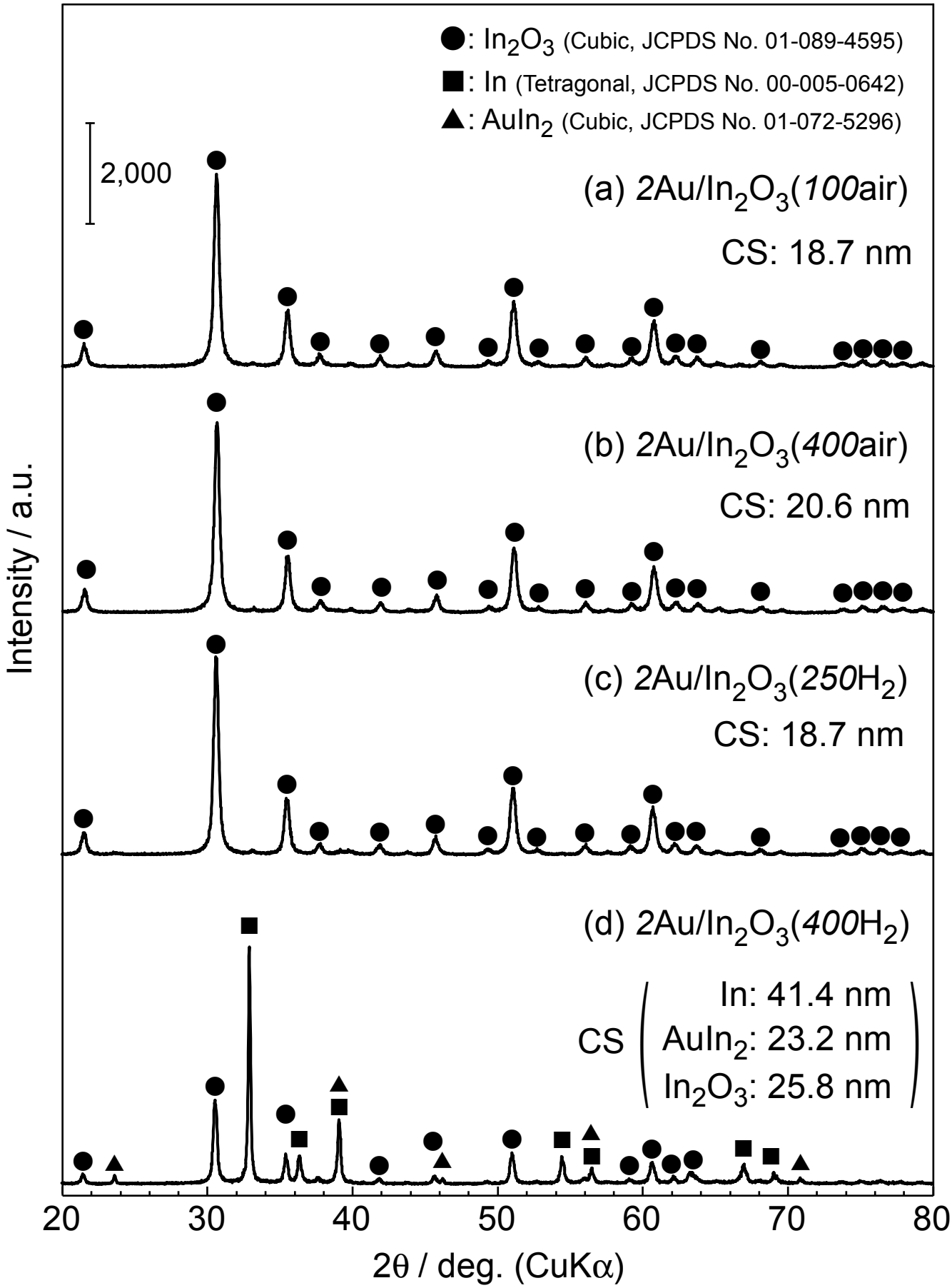

Figure 12. XRD patterns of 2Au/In_2O_3(*T*m) powders treated at several conditions, together with the crystallite size of In, In_2O_3 and $AuIn_2$.

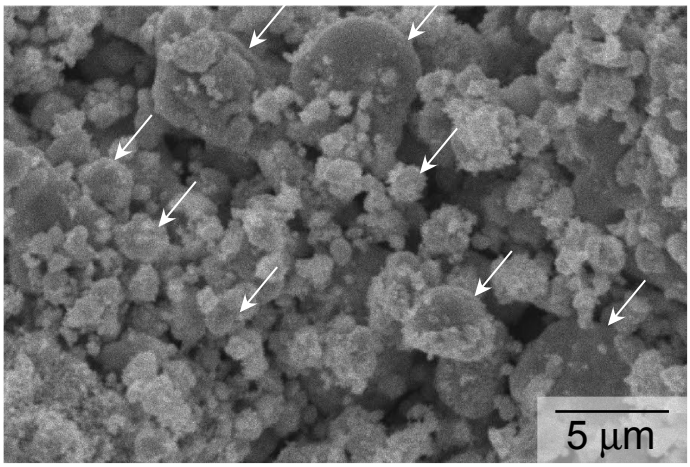

Figure 13. SEM image of the *2.0*Au/In_2O_3(*400*H_2) powder. Representative In metal or $AuIn_2$ particles were marked by arrowheads.

(a) *2.0*Au/In_2O_3(*100*air) powder

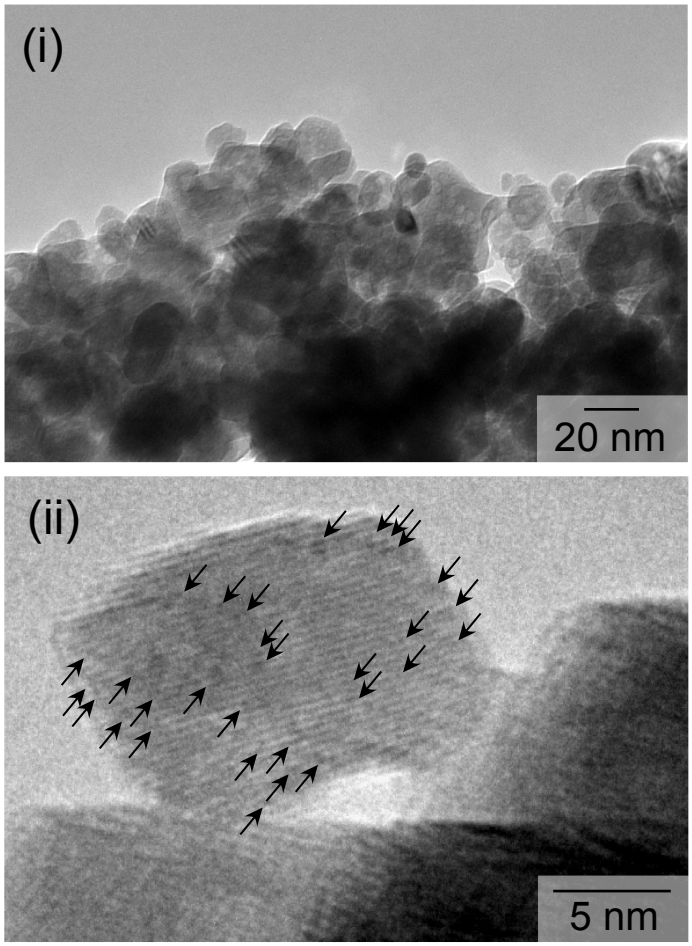

(b) *2.0*Au/In_2O_3(*250*H_2) powder

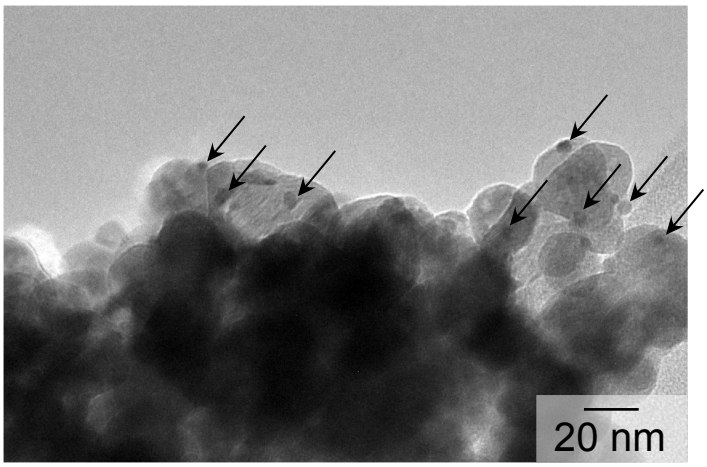

Figure 14. TEM images of (a) *2.0*Au/In_2O_3(*100*air) and (b) *2.0*Au/In_2O_3(*250*H_2) powder. The representative Au nanoparticles were marked by arrowheads.

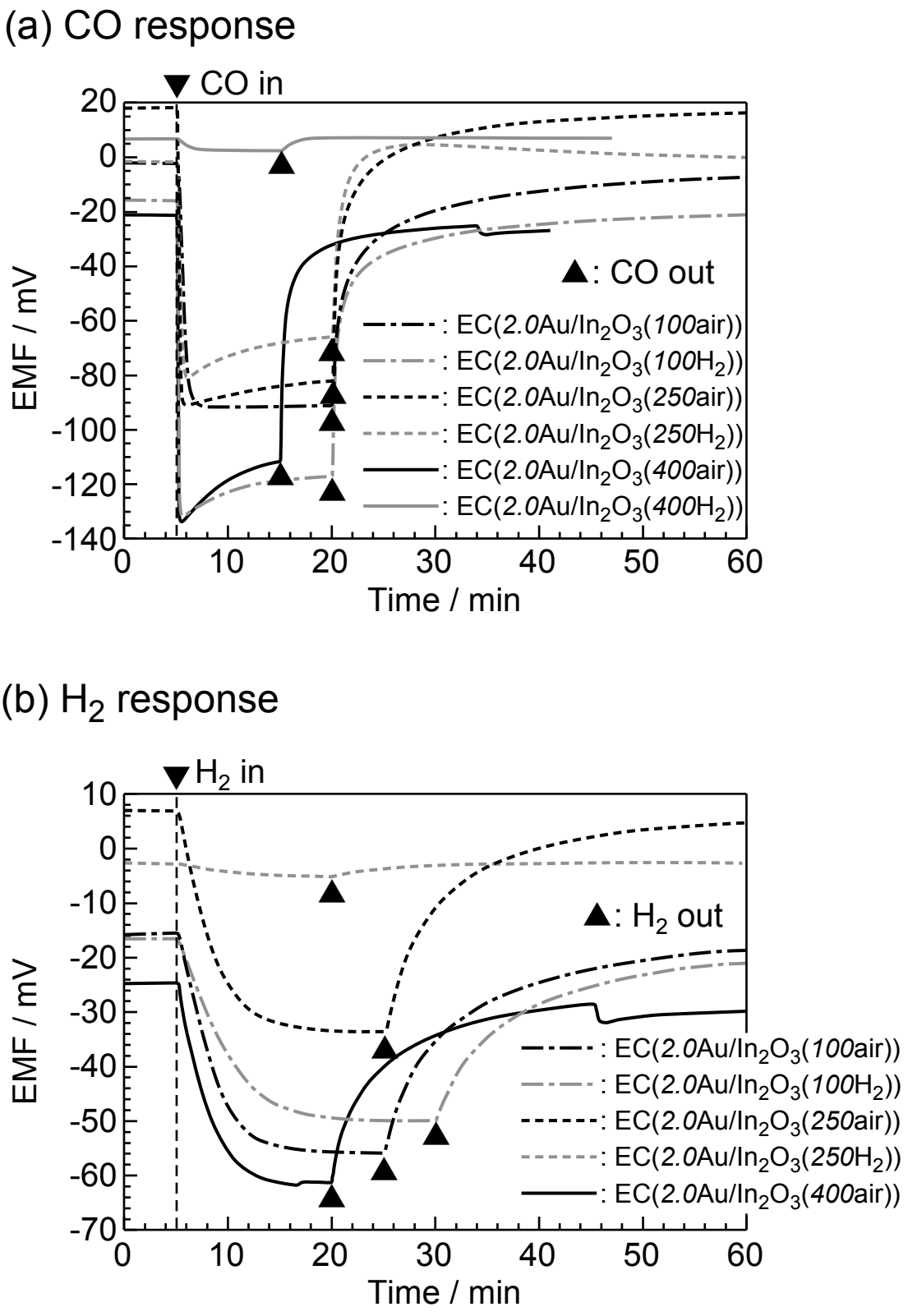

Figure 15. Response transients to 500 ppm (a) CO and (b) H_2 of EC(*2.0*Au/In_2O_3(*T*m)) in wet synthetic air at 30°C (57%RH).

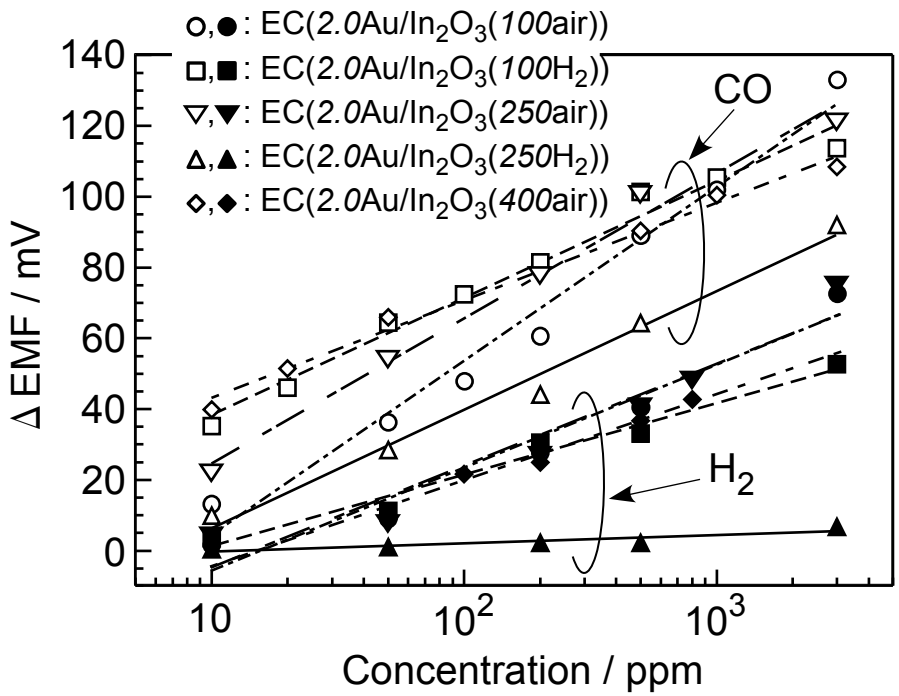

Figure 16. CO and H_2 concentration dependence of the responses of EC(*2.0*Au/In_2O_3(*T*m)) sensors in wet synthetic air at 30°C (57%RH).

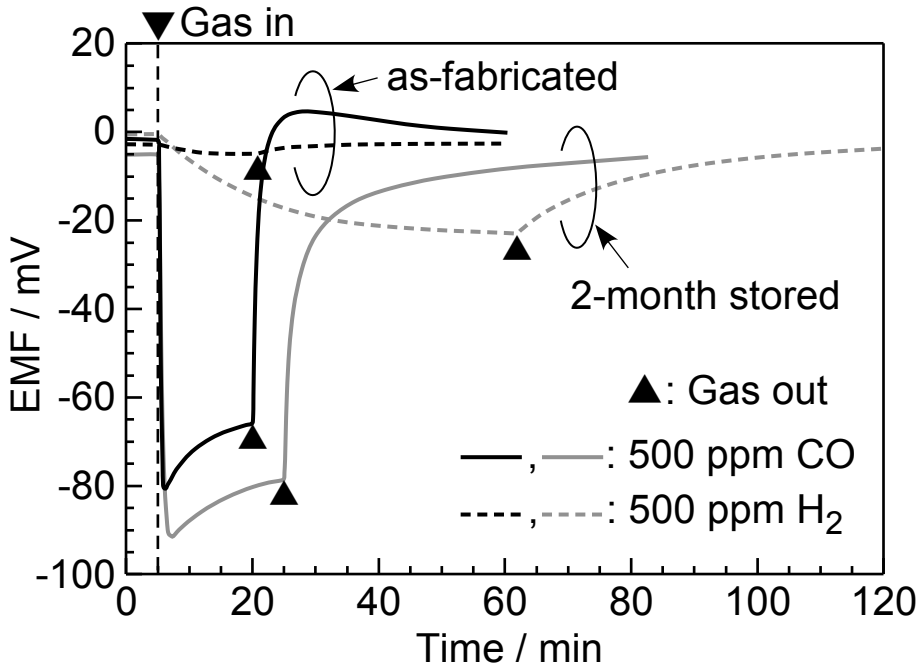

Figure 17. Response transients of fresh and 2 months stored EC(*2.0*Au/In_2O_3(*250*H_2)) sensor to 500 ppm CO and 500 ppm H_2 in wet synthetic air at 30°C (57%RH).

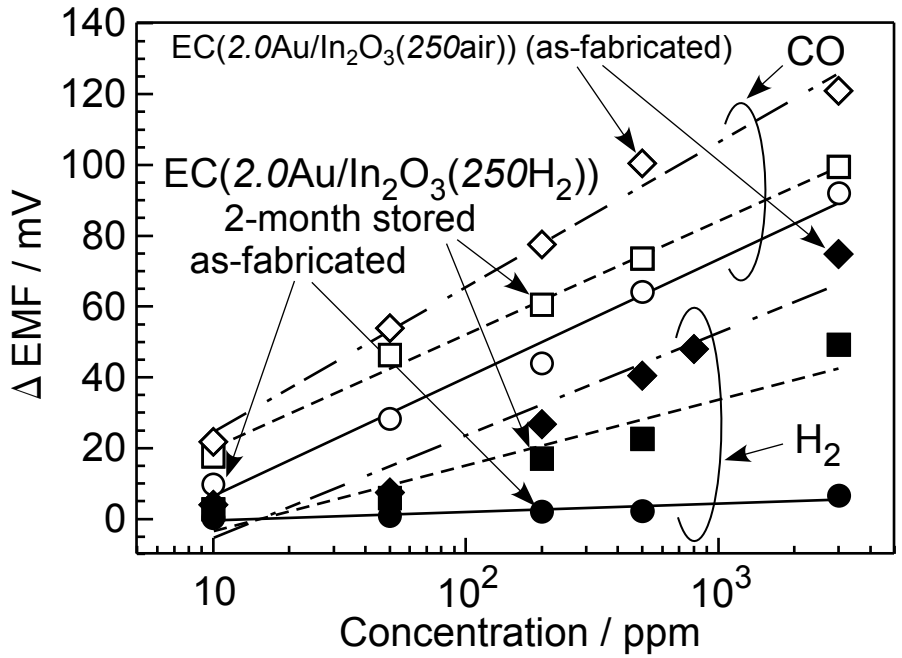

Figure 18. CO and H_2 concentration dependence of the responses of fresh and 2 months stored EC(*2.0*Au/In_2O_3(*250*H_2)) sensor in wet synthetic air at 30°C (57%RH), together with those of the fresh EC(*2.0*Au/In_2O_3(*250*air)) sensor.